

A DENSITY FUNCTIONAL THEORY INVESTIGATION OF  
GRAPHENE-BASED MATERIALS

A THESIS SUBMITTED TO  
THE GRADUATE SCHOOL OF NATURAL AND APPLIED SCIENCES  
OF  
MIDDLE EAST TECHNICAL UNIVERSITY

BY

CEREN SIBEL SAYIN

IN PARTIAL FULFILLMENT OF THE REQUIREMENTS  
FOR  
THE DEGREE OF DOCTOR OF PHILOSOPHY  
IN  
PHYSICS

SEPTEMBER 2014



Approval of the thesis:

**A DENSITY FUNCTIONAL THEORY INVESTIGATION OF  
GRAPHENE-BASED MATERIALS**

submitted by **CEREN SIBEL SAYIN** in partial fulfillment of the requirements for the degree of **Doctor of Philosophy in Physics Department, Middle East Technical University** by,

Prof. Dr. Canan Özgen  
Dean, Graduate School of **Natural and Applied Sciences**

\_\_\_\_\_

Prof. Dr. Mehmet T. Zeyrek  
Head of Department, **Physics**

\_\_\_\_\_

Assoc. Prof. Dr. Hande Toffoli  
Supervisor, **Physics Department, METU**

\_\_\_\_\_

**Examining Committee Members:**

Prof. Dr. Oğuz Gülseren  
Physics Department, Bilkent University

\_\_\_\_\_

Assoc. Prof. Dr. Hande Toffoli  
Physics Department, METU

\_\_\_\_\_

Prof. Dr. Şenay Katırcıoğlu  
Physics Department, METU

\_\_\_\_\_

Prof. Dr. Ahmet Oral  
Physics Department, METU

\_\_\_\_\_

Prof. Dr. Şinasi Ellialtıoğlu  
Basic Sciences Unit, TED University

\_\_\_\_\_

**Date:**

\_\_\_\_\_

**I hereby declare that all information in this document has been obtained and presented in accordance with academic rules and ethical conduct. I also declare that, as required by these rules and conduct, I have fully cited and referenced all material and results that are not original to this work.**

Name, Last Name: CEREN SIBEL SAYIN

Signature :

# **ABSTRACT**

## **A DENSITY FUNCTIONAL THEORY INVESTIGATION OF GRAPHENE-BASED MATERIALS**

Sayın, Ceren Sibel

Ph.D., Department of Physics

Supervisor : Assoc. Prof. Dr. Hande Toffoli

September 2014, 65 pages

Employability of graphene-based materials in various technological applications in order to exploit its exceptional properties is achieved/improved via their interactions with various atoms, molecules, nanostructures and surfaces. In this thesis, the interaction of cyclohexane and derived molecules, carbon nanotubes and metallic surfaces with both pristine and defected graphene structures are investigated using density functional theory.

Keywords: Graphene, Carbon Nanotubes, Cyclohexane, Density Functional Theory

# ÖZ

## GRAFEN BAZLI MALZEMELERİN YOĞUNLUK FONKSİYONELİ TEORİSİYLE İNCELENMESİ

Sayın, Ceren Sibel  
Doktora, Fizik Bölümü  
Tez Yöneticisi : Doç. Dr. Hande Toffoli

Eylül 2014 , 65 sayfa

Grafen bazlı malzemelerin olağanüstü özelliklerinden yararlanmayı amaçlayan çeşitli teknolojik uygulamalarda, bu yapıların kullanımı çeşitli atomlar, moleküller, nano yapılar ve yüzeyler ile etkileşimi yoluyla gerçekleştirilir ve geliştirilir. Bu tezde, sikloheksan ve türevi halkalı moleküller, karbon nanotüpler ve metalik yüzeylerin hem bozulmamış hem de kusurlu grafen yapıları etkileşimi yoğunluk fonksiyoneli teorisi kullanılarak incelenmiştir.

Anahtar Kelimeler: Grafen, Karbon Nanotüpler, Sikloheksan, Yoğunluk Fonksiyoneli Teorisi

To my family

## ACKNOWLEDGMENTS

First of all, I would like to express my heartfelt gratitude to my advisor Assoc. Prof. Dr. Hande Toffoli for offering her patient and insightful guidance throughout many years we worked together.

I would like to extend my gratitudes to Prof. Dr. Oğuz Gülseren, Prof. Dr. Şenay Katırcıoğlu and Prof. Dr. Şinasi Ellialtıoğlu for the helpful discussions which greatly supported this work.

I owe many thanks to my friends: Kıvılcım Başak Vural, Mustafa Tek, Merve Demirtaş, Çağan Aksak, Selma Şenozan, Okan Karaca Orhan, Mehtap Özbey, Gül Çorbacıoğlu, Cem Lider, Suat Dengiz, Miraç Serim, Cesim Dumlu, Nader Ghazanfari, Mehmet Ali Olpak, Turan Birol and Emre Taşçı. I would like to thank Taylan Takan who shared a large part of this journey with me. My special thanks are for Yakup Pekön who brightened my darkest days. I am thankful to many other fellow students and staff of the METU Physics Department.

My mother and other members of my family incessantly offered their unconditional love and support, I am grateful to all of them.



# TABLE OF CONTENTS

ABSTRACT . . . . .	v
ÖZ . . . . .	vi
ACKNOWLEDGMENTS . . . . .	viii
TABLE OF CONTENTS . . . . .	ix
LIST OF TABLES . . . . .	xii
LIST OF FIGURES . . . . .	xiii
CHAPTERS	
1 INTRODUCTION . . . . .	1
1.1 Electronic Structure of Graphene . . . . .	4
1.2 Defects on Graphene . . . . .	6
2 THEORETICAL METHODS . . . . .	11
2.1 Many-Body Hamiltonian . . . . .	11
2.2 Born-Oppenheimer (Adiabatic) Approximation . . . . .	12
2.3 Hartree-Fock Method/Slater Determinants . . . . .	13
2.4 Density Functional Theory . . . . .	13
2.4.1 The Variational Principle . . . . .	14

2.4.2	Hohenberg-Kohn Theorems . . . . .	14
2.5	Kohn-Sham Equations . . . . .	15
2.5.1	Exchange–Correlation Functionals . . . . .	16
2.5.2	Plane Wave Expansion . . . . .	17
2.5.3	Pseudopotentials . . . . .	20
2.5.4	Pseudopotential Generation . . . . .	21
2.6	Self-Consistency Cycle . . . . .	22
2.7	van-der Waals Interaction . . . . .	23
2.7.1	Benchmarking vdW functionals . . . . .	26
3	CARBON NANOTUBES ON GRAPHENE ON METALS . . . . .	29
3.1	Computational Details . . . . .	29
3.2	CNTs on Graphene . . . . .	30
3.3	Graphene/Metal Interface . . . . .	35
3.4	CNTs on Graphene on Metals . . . . .	37
4	INTERACTION OF IDEAL AND DEFECTED GRAPHENE WITH CYCLOHEXANES . . . . .	41
4.1	Computational Details . . . . .	41
4.2	$C_6H_{12}$ , $C_6H_{11}^*$ and $C_6H_{10}$ . . . . .	42
4.3	Molecules on Ideal Graphene . . . . .	43
4.4	Defect-Bonded Molecules . . . . .	47
4.5	Molecules on N-Doped Graphene . . . . .	50
5	CONCLUSION . . . . .	55

REFERENCES . . . . .	57
CURRICULUM VITAE . . . . .	65

## LIST OF TABLES

### TABLES

Table 2.1	Optimized lattice constants for graphene with different functionals . . . . .	26
Table 2.2	Binding energies and distances for graphite calculated with different functionals. . . . .	27
Table 3.1	The equilibrium bond lengths and the binding energy per length for the adsorption of CNT(6,0) and CNT(8,0) on graphene through van-der Waals, single and double C-C bonds. . . . .	33
Table 3.2	Experimental bulk lattice constants, surface lattice constants and surface-graphene percent mismatches calculated with different functionals for Cu and Ni. . . . .	36
Table 4.1	Distances and binding energies of C <sub>6</sub> H <sub>12</sub> and C <sub>6</sub> H <sub>11</sub> * on ideal graphene layer at different sites. . . . .	46
Table 4.2	Summary of the binding energies $E_b$ , distances $d$ of the molecules adsorbed on pristine graphene, graphene with a single vacancy, graphene with a C adatom and N-Doped graphene . . . . .	54

## LIST OF FIGURES

### FIGURES

Figure 1.1	The real and reciprocal lattices of graphene . . . . .	5
Figure 1.2	The band structure graphene obtained from tight-binding theory. . .	6
Figure 1.3	The band structure and DOS plots of graphene obtained from density functional theory. . . . .	6
Figure 1.4	Charge density plots for pristine graphene (a), graphene with a single vacancy (majority spin) (b), a single C adatom (c), and N-doped graphene (d). . . . .	8
Figure 1.5	Band structure and DOS plots for graphene with a single vacancy (a), a single C adatom (b) and N-doped graphene (c). . . . .	9
Figure 2.1	All electron and pseudopotential wave functions for the c09x and revpbe functionals. . . . .	23
Figure 2.2	The binding energy difference plots for different functionals for graphite(a) and bilayer graphene(b). . . . .	28
Figure 3.1	The binding energy vs. distance plots for a horizontally aligned (8,0) CNT on graphene calculated with PBE-GGA and vdW-DF2 <sup>c09</sup> functionals. . . . .	31
Figure 3.2	The on-top (left) and shifted (right) geometries of a CNT on graphene. . . . .	33
Figure 3.3	The optimized structures and density of states plots for a CNT(8,0) on graphene for van-der Waals interaction (a), single C-C bonds (b) and double C-C bonds (c). . . . .	34
Figure 3.4	The on-top geometry of graphene on Ni(111) and the band structure of the graphene/Ni(111) system. . . . .	37
Figure 3.5	The relaxed configurations and band structures of graphene on Cu(111) calculated with the lattice parameter of graphene (top) and lattice parameter of the metal (bottom). . . . .	38

Figure 3.6 The CNT(8,0) interacting through van-der Waals forces (top) and a single C–C bond (bottom) with graphene on Cu(111). . . . .	39
Figure 4.1 Relaxed structures of the (a) $C_6H_{12}$ , (b) $C_6H_{11}^*$ and (c) $C_6H_{10}$ molecules along with the HOMO (middle panel) and LUMO (lower panel) orbitals . . . . .	44
Figure 4.2 The $C_6H_{12}$ molecule on pristine graphene with (a) 1/9 ML and (b) 1/36 ML concentrations. . . . .	45
Figure 4.3 Different initial configurations for $C_6H_{12}$ on pristine graphene. . . . .	47
Figure 4.4 Geometry and band structure of $C_6H_{12}$ (a), $C_6H_{11}^*$ (b) and $C_6H_{10}$ (c) on pristine graphene . . . . .	48
Figure 4.5 Geometry and band structure of, $C_6H_{12}$ (a), $C_6H_{11}^*$ (b) and $C_6H_{10}$ (c) interacting with a single vacancy. . . . .	51
Figure 4.6 Geometry and band structure of, $C_6H_{12}$ (a), $C_6H_{11}^*$ (b) and $C_6H_{10}$ (c) interacting with a single C adatom. . . . .	52
Figure 4.7 Geometry and band structure (a) $C_6H_{12}$ , (b) $C_6H_{11}^*$ and (c) and $C_6H_{10}$ interacting with N-doped graphene. . . . .	53

# CHAPTER 1

## INTRODUCTION

The two-dimensional graphene and its derivatives such as single-dimensional carbon nanotubes and carbon buckyballs attract a deserved attention due to their exceptional properties [52, 34, 60]. Behavior of electrons in graphene like massless Dirac fermions manifested in the linear dispersion of the bands makes graphene a laboratory for various 2+1 dimensional QED phenomena [38, 13]. As for practical applications, owing to high carrier mobility and scalability to small sizes, graphene based nanostructures are promising candidates to replace conventional semiconductors in field-effect transistors and to be employed in other areas like solar-cells, sensors, actuator devices [67, 62, 64, 75, 33].

Advances in the fabrication and processing of graphene [53] has greatly expanded its domain of practical utility in the last decade. In a short span of time, graphene has gone from being a novel source of fascinating physical phenomena [10, 65] to sophisticated applications in various fields including optics, catalysis and device technology [77, 36, 31, 57]. Owing to its unique, defect-free  $sp^2$  network structure, graphene possesses unusually high carrier mobility, thermal conductivity and mechanical strength. The distinguishing feature of the electronic structure is the occurrence of double cones in its band structure at the six Fermi points in its hexagonal Brillouin zone, referred to as Dirac cones. Contributed by the delocalized  $\pi - \pi^*$  orbitals, the apices of the Dirac cones touch at a single point resulting in a linear electronic dispersion and a zero density of states at the Fermi level.

Miniaturized device technology relies on the tunability of the amount of charge carriers and the band gap. While the high mobility of graphene is desirable, the lack of

a band gap is a drawback in such applications as graphene-based field-effect transistors, which require a high on/off current ratio [77]. Much effort has therefore been invested in developing the ability to control the location of the Fermi level and the opening of a band gap. A striking example to this search has been given by Coletti *et al* [14] where the Fermi level of a graphene sheet, already n-doped by the SiO<sub>2</sub> substrate underneath was gradually restored to its original location at the Dirac point by controllably reversing the charge transfer via an increased coverage of the surface by F4-TCNQ molecules. Beside device applications, controlling the amount of charge on the graphene sheet is also important from the point of view of catalytic activity, photocatalytic and photovoltaic applications. A study by Qian *et al.* [56] showed that by attaching 1,2-ethylenediamine groups to the edges of graphene quantum dots, the fluorescence quantum yield was increased 17-fold without increasing biotoxicity. Numerous methods have been developed to achieve control over the band structure including application of mechanical strain [7, 5], substrate doping [14], electric field doping [69] and confinement via nanoribbon formation [10].

Chemical functionalization of graphene is a versatile functionalization technique employed in a variety of applications including band gap engineering, superior gas sensing abilities, increased hydrogen storage capacity, synthesis of graphene-derived nanostructures, prevention of agglomeration and stacking of graphene layers, and induction of magnetic properties for use in spintronics [61, 23, 9, 41, 48]. The species used in the chemical functionalization of graphene range in size and variety from single atoms [1, 37], all the way to large polymers [47]. Depending on the application at hand, functionalization may be achieved via covalent or noncovalent bonding of the molecules to the network. Covalent bonding is usually accompanied by the destruction of the linear dispersion around the Fermi points and the opening of a band gap at the Fermi points due to the introduction of sp<sup>3</sup> bonds. Noncovalent functionalization, on the other hand, usually relies on weak dispersive forces and often leaves the band structure unchanged. A charge transfer may nonetheless occur even for noncovalent bonding, moving the Fermi level above or below the Fermi points, thereby changing the doping level. Physisorption and chemisorption of the same functionalizing species may also be observed simultaneously through the occurrence of different reaction steps during the functionalization process as noted by Englert *et al.* [21] in a



study using thermal gravimetric analysis coupled to mass spectroscopy (TGA/MS). This study showed that graphene quantum dots functionalized by 4-TBD molecules lose mass at two different temperatures, the lower ( $\sim 210^\circ$ ) corresponding to the physisorbed species and the higher ( $\sim 480^\circ$ ) corresponding to the cleavage of covalent bonds.

In this work, density functional theory (DFT) which is a powerful tool in the prediction of structural and electronic properties of nanostructures based on first principles calculations is employed. In the first part, an analysis of the interaction of single walled carbon nanotubes (CNTs) with isolated graphene sheets, the adsorption of graphene on metallic surfaces and interaction of CNTs with graphene supported by metals is conducted. CNT/graphene hybrid films were shown to demonstrate enhanced features as transparent conductors and supercapacitors [70, 80]. All-carbon FET devices with semiconducting CNT channels were successfully manufactured where source, drain and gate electrodes are made of graphene sheets [35, 45, 81]. The graphene-metal interface bears great importance due to the essential role of metals in most applications: they are used as catalyst substrates for high quality sample production, the probes of characterization devices and electrodes in electronic devices are metallic. The lattice constant of graphene matches very well with the surface lattice parameters of some metals such as Ni(111) and Cu(111) which allows graphene to assume a commensurate single adsorption geometry. With others such as Ru(0001), a lattice mismatch causes formation of different local adsorption structures or rotated registries which result in Moire superlattices. The varying interaction strengths causes corrugations in the graphene layer which allows Moire patterns to be used as templates for preferential adsorption sites [76, 4].

Secondly, the interaction of cyclohexane and derived molecules with ideal and defected graphene structures has been studied. Cyclohexane (c-hexane,  $C_6H_{12}$ ) is a monocyclic hydrocarbon where the  $sp^3$  hybridized carbon atoms are each bonded to two neighboring C atoms and two H atoms. Cyclohexane is conventionally synthesized from hydrogenation of benzene and is produced on large industrial scales primarily to employ in the production of adipic acid which is a nylon intermediate and secondarily as a non-polar solvent [46]. Interaction between cyclohexane (and its dehydrogenated or oxygenated derivatives) and graphene based materials has been spo-

radically explored in experimental and theoretical literature. According to an experimental study conducted by Yu *et al.* [81], N-doped carbon nanotubes (CNTs) display catalytic activity towards the anaerobic oxidation of cyclohexane. Yang *et al.* [79] recently developed a recipe for extracting graphene sheets from a graphite sample making use of the weak dispersive interaction between cyclohexane and the graphene basal plane. Bittner *et al.* [6] and Díaz *et al.* [19], on the other hand, probe binding energies of non-cyclic and cyclic molecules on CNTs including cyclohexane and cyclohexene from a gas adsorption point of view. In a DFT study, Zhao *et al.* [84] studied the binding energy and charge transfer of  $C_6H_6$ ,  $C_6H_{12}$  and 2,3-dichloro-5,6-dicyano-1,4-benzoquinone (DDQ) with a single-walled CNT.  $C_6H_{12}$  was found to bind slightly more strongly to the surface even though all molecule-CNT interactions were of dispersive nature. Finally, another DFT study by Yang *et al.* [79] shed light on the CNT-catalyzed oxidation of  $C_6H_{12}$  with molecular oxygen. In spite of the important potential applications mentioned in these studies, a thorough systematic atomic scale examination is missing.

This thesis is structured as follows: In the introduction, properties of ideal and defected graphene are briefly mentioned. The theoretical background is explained in the following chapter. In Chapter 3, the results on the CNT/graphene, CNT/metal and CNT/graphene/metal interfaces are presented. Chapter 4 is devoted to the calculations on the interaction of cyclohexane molecules with pristine and defected graphene layers. Conclusions are summarized in the last chapter. Throughout this work, all the calculations were performed using the open-source Quantum Espresso code [24] which is based on plane-wave pseudopotential density functional theory. All the figures were generated using the XCrYsden visualisation program [40].

## 1.1 Electronic Structure of Graphene

The unit cell of the two-dimensional honey-comb lattice of a graphene sheet is a hexagon containing two atoms in the basis. The primitive lattice vectors  $\mathbf{a}_1, \mathbf{a}_2$  and the corresponding reciprocal vectors  $\mathbf{b}_1, \mathbf{b}_2$  found from the relation  $\mathbf{a}_i \cdot \mathbf{b}_j = 2\pi \times \delta_{ij}$

are:

$$\begin{aligned} \mathbf{a}_1 &= \frac{a}{2}(3, \sqrt{3}) & \mathbf{a}_2 &= \frac{a}{2}(3, -\sqrt{3}) \\ \mathbf{b}_1 &= \frac{2\pi}{3a}(1, \sqrt{3}) & \mathbf{b}_2 &= \frac{2\pi}{3a}(1, -\sqrt{3}) \end{aligned} \quad (1.1)$$

where  $a$  is the interatomic distance of  $1.42 \text{ \AA}$  corresponding to a lattice constant of  $2.46 \text{ \AA}$ . The real space representation of graphene with the primitive lattice vectors and the first Brillouin zone with the reciprocal lattice vectors along with special K-points are shown in Figure 1.1.

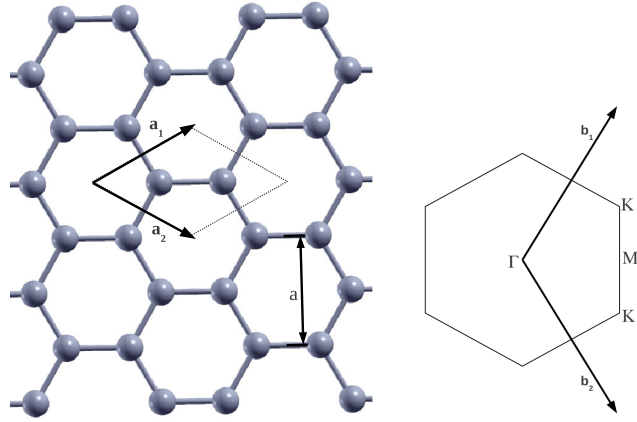


Figure 1.1: The real and reciprocal lattices of graphene

The band structure of graphene was first predicted by Wallace in 1946 [73]. Graphene bands cross the Fermi level at the Dirac points  $\mathbf{K}$  and  $\mathbf{K}'$  which makes it a zero-gap semiconductor. They are called Dirac points as the linear dispersion relation of the bands at these points mimics the Dirac equation. They are located at:

$$\mathbf{K} = \frac{2\pi}{3a}\left(1, \frac{1}{\sqrt{3}}\right) \quad \mathbf{K}' = \frac{2\pi}{3a}\left(1, -\frac{1}{\sqrt{3}}\right) \quad (1.2)$$

The linear dispersion relation from these points obtained from a tight-binding approximation is:

$$E_{\pm}(\mathbf{k}) \simeq \epsilon \pm \hbar v_F(\mathbf{k}) \quad (1.3)$$

The three dimensional plot of graphene band structure obtained from the tight-binding theory is seen in Figure 1.2 and the two dimensional band-structure along with the DOS obtained from ab initio calculations is presented in Figure 2.2.

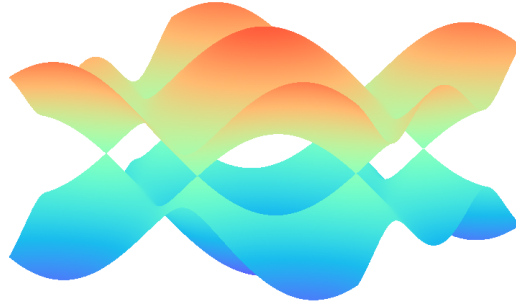


Figure 1.2: The band structure graphene obtained from tight-binding theory.

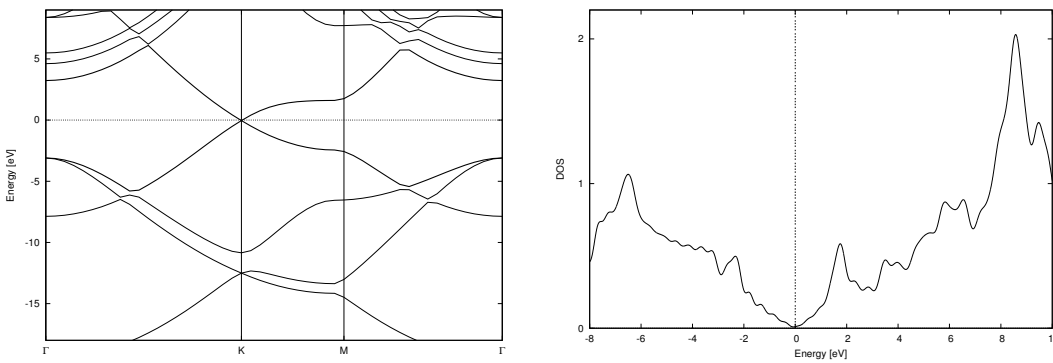


Figure 1.3: The band structure and DOS plots of graphene obtained from density functional theory.

## 1.2 Defects on Graphene

In order to mitigate the chemical inertness of graphene, defects and impurities can be introduced in the network to facilitate functionalization [8, 83]. Point defects, such as single or double vacancies and adatoms locally alter the electronic structure which can act as functionalization centers [16, 74]. Due to high formation energies, such defects have negligible concentration in graphene produced through standard sample growth processes, nonetheless, controlled defect creation is possible via methods such as particle irradiation and chemical treatment [2]. Foreign atoms such as B and N may also be substitutionally introduced to act as charge acceptors and donors to modify reactivity [58].

In this thesis, defected graphene structures with a single vacancy, a single carbon

adatom and a substitutionally doped Nitrogen atom are considered.

The defect formation energies are calculated from:

$$E_{def} = E_{pristine} - E_{defected} + \mu_C \quad (1.4)$$

where  $E_{pristine}$  is the total energy of the pristine graphene sheet,  $E_{defected}$  is the total energy of defected graphene and  $\mu_C$  is the chemical potential of a Carbon atom calculated from graphite which is negative for a vacancy and positive for an adatom. This chemical potential was taken as  $E_{ideal}/N$  with  $N$  being the number of C atoms in the unit cell. From this formula, single vacancy formation energy and adatom binding energy are calculated to be 7.77 eV and 1.62 eV respectively which are both in good agreement with previous theoretical and experimental results [68].

Some important aspects of a single vacancy on graphene are still debated; such as whether the atoms around the vacancy remain planar or non-planar and the nature of the magnetic properties of the defective structure [54, 51]. Our spin-polarized and unpolarized calculations both yielded a flat structure displaying Jahn-Teller distortion. The spin-polarized calculation is energetically more favorable by 0.4 eV and yielded a total magnetic moment of  $1.45 \mu_B$  per cell calculated with the GGA. For a carbon adatom, we found that the most stable geometry is the bridge position where the additional C atom resides on top of the mid-point of a carbon bond of graphene in accordance with previous studies. C adatom is covalently bonded to graphene through two equivalent C-C bonds with bond length  $1.50 \text{ \AA}$ . Contrary to the single vacancy case, the spin resolved computation for the adatom gave zero net magnetic moment.

The substitution energy for N is calculated using:

$$E_{sub} = E_{N-doped} - (E_{pristine} - \mu_C) + \mu_N \quad (1.5)$$

where  $\mu_N$  is the chemical potential of Nitrogen calculated by considering the  $N_2$  dimer. This energy is computed to be 0.75 eV.

Upon N substitution the atoms of the graphene layer remain coplanar, while the bond length of the three C-N bonds around N slightly shrink by  $0.1 \text{ \AA}$  to  $1.41 \text{ \AA}$ . A spin-polarized calculation for the N-doped graphene yielded a magnetization of  $0.01 \mu_B$  per cell and the structure remain unchanged. The small magnetization is

neglected and the calculations involving N-doped graphene were conducted without spin-polarization. Bare graphene with a nitrogen impurity is negatively doped which is reflected in the band structure as a downward shift.

The relaxed pristine and defected structures along with charge density plots are presented in Figure 1.4. The band structures and density of state (DOS) plots of defected graphene structures are seen in Figure 1.5.

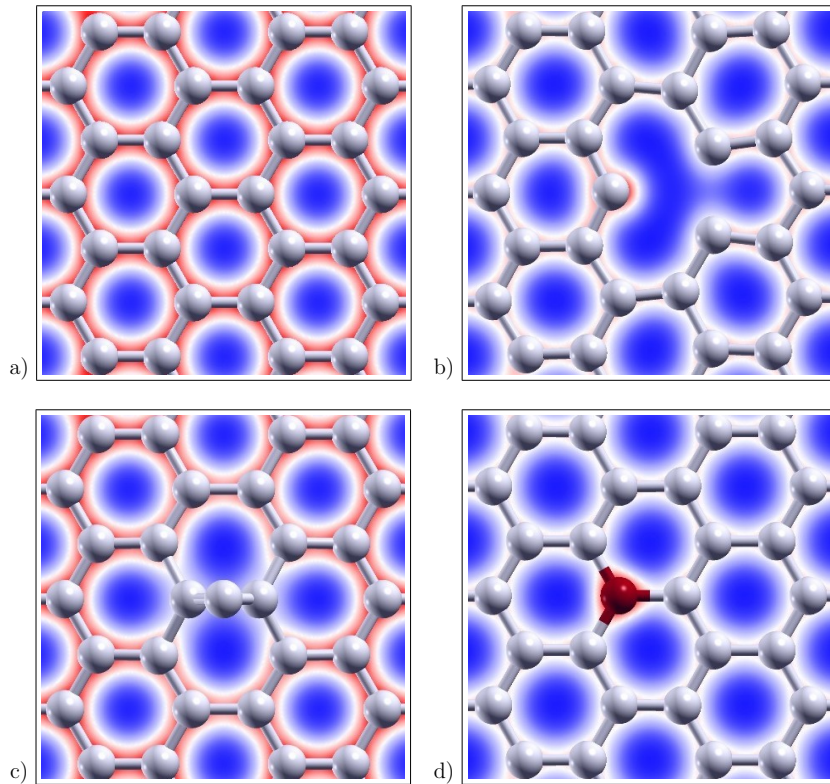


Figure 1.4: Charge density plots for pristine graphene (a), graphene with a single vacancy (majority spin) (b), a single C adatom (c), and N-doped graphene (d).

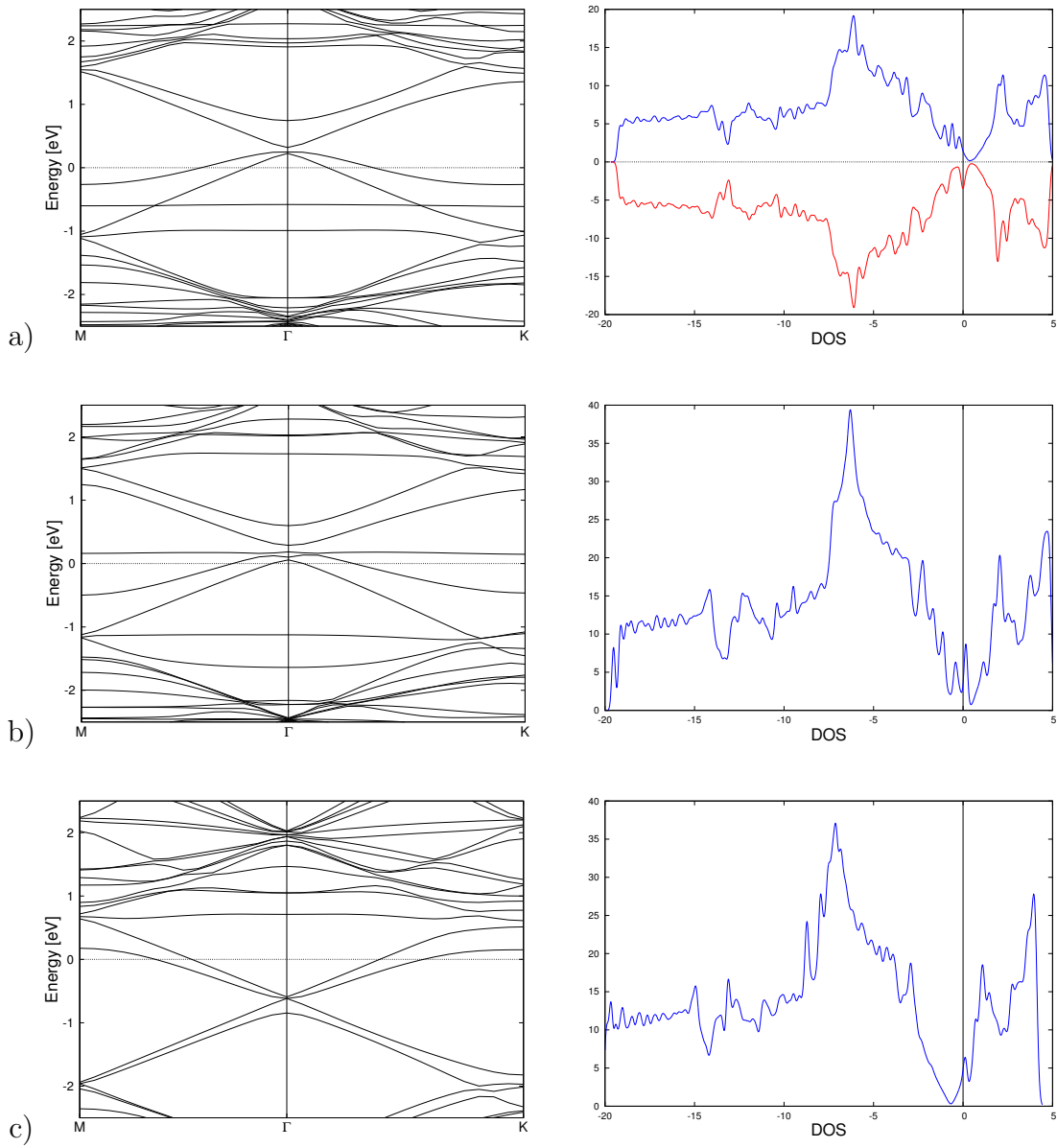


Figure 1.5: Band structure and DOS plots for graphene with a single vacancy (a), a single C adatom (b) and N-doped graphene (c).





## CHAPTER 2

### THEORETICAL METHODS

#### 2.1 Many-Body Hamiltonian

In principle, all stationary information about any material can be extracted from the time-independent Schrödinger equation (neglecting relativistic effects):

$$\hat{\mathbf{H}}\psi = E\psi \quad (2.1)$$

The non-relativistic Hamiltonian for a system of  $N$  electrons with corresponding set of coordinates  $\mathbf{r} \equiv \{\mathbf{r}_i, i = 1, \dots, N\}$  and  $P$  nuclei with coordinates  $\mathbf{R} \equiv \{\mathbf{R}_I, I = 1, \dots, P\}$  and nuclear charge  $Z_I$  is:

$$\begin{aligned} \hat{\mathbf{H}} = & -\frac{\hbar^2}{2m_e} \sum_i^N \nabla_i^2 - \frac{\hbar^2}{2} \sum_I^P \frac{\nabla_I^2}{M_I} + \frac{e^2}{4\pi\epsilon_0} \left( \frac{1}{2} \sum_I^P \sum_{J \neq I}^P \frac{Z_I Z_J}{|\mathbf{R}_I - \mathbf{R}_J|} + \right. \\ & \left. + \frac{1}{2} \sum_i^N \sum_{j \neq i}^N \frac{1}{|\mathbf{r}_i - \mathbf{r}_j|} - \sum_i^N \sum_I^P \frac{Z_I}{|\mathbf{r}_i - \mathbf{R}_I|} \right) \quad (2.2) \end{aligned}$$

In atomic units ( $e = m_e = \hbar = 1$ ), the Hamiltonian becomes:

$$\begin{aligned} \hat{\mathbf{H}} = & -\frac{1}{2} \sum_i^N \nabla_i^2 - \frac{1}{2} \sum_I^P \frac{\nabla_I^2}{M_I} + \frac{1}{4\pi\epsilon_0} \left( \frac{1}{2} \sum_I^P \sum_{J \neq I}^P \frac{Z_I Z_J}{|\mathbf{R}_I - \mathbf{R}_J|} + \right. \\ & \left. + \frac{1}{2} \sum_i^N \sum_{j \neq i}^N \frac{1}{|\mathbf{r}_i - \mathbf{r}_j|} - \sum_i^N \sum_I^P \frac{Z_I}{|\mathbf{r}_i - \mathbf{R}_I|} \right) \quad (2.3) \end{aligned}$$

which can be written compactly as:

$$\hat{\mathbf{H}} = \hat{\mathbf{T}}_e(\mathbf{r}) + \hat{\mathbf{T}}_N(\mathbf{R}) + \hat{\mathbf{V}}_{ee}(\mathbf{r}) + \hat{\mathbf{V}}_{NN}(\mathbf{R}) + \hat{\mathbf{V}}_{eN}(\mathbf{r}, \mathbf{R}) \quad (2.4)$$

The corresponding total wave function of the Hamiltonian is  $\psi(\mathbf{r}_1, \dots, \mathbf{r}_N, \mathbf{R}_1, \dots, \mathbf{R}_N)$ .

## 2.2 Born-Oppenheimer (Adiabatic) Approximation

Obtaining exact solutions for the many-body Hamiltonian especially for large systems is an impossible task. Firstly due to entangled states which forbid the wave function to be separated into single-particle components, and secondly due to the immeasurable computational load such a task requires. Thus, several approximations are needed.

The first of these is the Born–Oppenheimer approximation which allows the wave function to be broken into electronic and nuclear components. Basically, it states that the instantaneous electronic states are not affected by the motion of the much heavier nuclei. As the nuclear mass  $M_I$  becomes very large, the associated kinetic energy term,  $\hat{\mathbf{T}}_I$ , can be ignored. Also, the nucleus–nucleus interaction term,  $E_{II}$ , only has a constant contribution which can be added afterwards.

Then the main problem at hand is to solve the Schrödinger equation for the electronic wave function  $\Psi_e(\mathbf{r}_i)$ , by using the Hamiltonian (in atomic units where  $\hbar = e = m_e = 4\pi\epsilon_0 = 1$ ):

$$\begin{aligned}\hat{\mathbf{H}}_e &= -\frac{1}{2} \sum_i \nabla_i^2 - \sum_{i,I} \frac{Z_I}{|\mathbf{r}_i - \mathbf{R}_I|} + \frac{1}{2} \sum_{i \neq j} \frac{1}{|\mathbf{r}_i - \mathbf{r}_j|} \\ &= \hat{\mathbf{T}} + \hat{\mathbf{V}}_{ext} + \hat{\mathbf{V}}_{int} .\end{aligned}\tag{2.5}$$

The nucleus–electron interaction, namely the external potential,  $\hat{\mathbf{V}}_{ext}$ , is a classical Coulombic interaction, whereas the electron–electron interaction,  $\hat{\mathbf{V}}_{int}$ , makes the wave function non–separable due to quantum mechanical exchange–correlation effects. Moreover, the dependence of  $\Psi_e(\mathbf{r}_i)$  on  $3N$  variables for an  $N$ -electron system still demands a vast computational capacity even for storage. This means that further approximations and different approaches are required for practical calculations. Systematic application of certain sets of approximations have been proven to yield successful results for certain classes of materials which gave rise to different methods of electronic structure calculations. For instance, wavefunction-based methods are convenient to use for small molecular systems, whereas density-based methods are mainly used for larger materials such as periodic crystals.

### 2.3 Hartree-Fock Method/Slater Determinants

An intuitive approximation for the wave function of a many electron system is the Hartree product which constructs the wave function from the individual single particle wave functions as  $\psi(\mathbf{r}) = \phi_1(\mathbf{r}_1)\phi_2(\mathbf{r}_2) \dots \phi_N(\mathbf{r}_N)$ . For a fermionic system, the wave function can be written as a normalized linear combination of Hartree products to satisfy the anti-symmetry property and given as a Slater determinant as:

$$\psi(\mathbf{r}) = \frac{1}{\sqrt{N!}} \begin{vmatrix} \phi_1(\mathbf{r}_1) & \phi_2(\mathbf{r}_1) & \dots & \phi_N(\mathbf{r}_1) \\ \phi_1(\mathbf{r}_2) & \phi_2(\mathbf{r}_2) & \dots & \phi_N(\mathbf{r}_2) \\ \vdots & \vdots & & \vdots \\ \phi_1(\mathbf{r}_N) & \phi_2(\mathbf{r}_N) & \dots & \phi_N(\mathbf{r}_N) \end{vmatrix} \quad (2.6)$$

### 2.4 Density Functional Theory

The electronic Hamiltonian suggests that any many-body system is basically a collection of interacting electrons moving in an external potential. Early quantum statistical models such as the Thomas–Fermi theory reasonably presumed that such a system could be analyzed using the density of electrons as the central variable instead of the wave function. Although these failed to accurately describe real systems, DFT followed the same approach and emerged as an exact theory. The density of particles  $n(\mathbf{r})$  gives probability density that any of the  $N$  electrons is at the position  $\mathbf{r}$ . It is obtained from the expectation value of the density operator  $\hat{n}(\mathbf{r}) = \sum_i^N \delta(\mathbf{r} - \mathbf{r}_i)$  as:

$$n(\mathbf{r}) = N \int \psi^*(\mathbf{r}, \mathbf{r}_2, \dots, \mathbf{r}_N) \psi(\mathbf{r}, \mathbf{r}_2, \dots, \mathbf{r}_N) d^3r_2 d^3r_3 \dots d^3r_N \quad (2.7)$$

The integral of the density give the total number of electrons  $\int n(\mathbf{r}) d^3r = N$  and the charge density for charge  $q$  is related to the particle density as  $\rho(\mathbf{r}) = qn(\mathbf{r})$ . Clearly, the density is determined by the wave function as any other observable. The question is to demonstrate the reverse case. Indeed, it was proven by Hohenberg and Kohn that the ground state wave function for a fixed external potential is a unique functional of the ground state density. They also showed that the energy corresponding to this ground state density acquires its minimum value which equals the ground state energy:

$$E_0 = \int V_{ext}(\mathbf{r})n(\mathbf{r})d\mathbf{r} + F[n(\mathbf{r})] . \quad (2.8)$$

In the above expression,  $F[n(\mathbf{r})]$  contains kinetic energy and electron–electron interaction terms. It is a universal functional as it is independent of the system in consideration.

### 2.4.1 The Variational Principle

The variational principle states that the ground state energy  $E_0$  of a system is always less than (or equal to if the trial function is the ground state wave function) the expectation value of the Hamiltonian calculated with a trial wave function  $\phi$ :

$$E_0 \leq \frac{\langle \phi | \hat{\mathbf{H}} | \phi \rangle}{\langle \phi | \phi \rangle} \quad (2.9)$$

Assuming that for the eigenvalue equation  $\hat{\mathbf{H}}\psi_n = E_n\psi_n$ ,  $E_n$  are the eigenvalues where  $E_0$  is the ground state,  $E_1$  is the first excited state etc. with  $E_0 < E_1 < E_2 \dots$  and  $\psi_n$  are the corresponding orthonormal eigenstates such that  $\langle \psi_n | \psi_m \rangle = \delta_{nm}$ . Then the trial wave function can be expanded in terms of  $\psi_n$  which form a complete basis set as  $|\phi\rangle = \sum_n c_n |\psi_n\rangle$  and the expectation value in 2.9 becomes:

$$\begin{aligned} \frac{\langle \phi | \hat{\mathbf{H}} | \phi \rangle}{\langle \phi | \phi \rangle} &= \frac{\sum_{nm} c_n c_m \langle \psi_n | \hat{\mathbf{H}} | \psi_m \rangle}{\sum_{nm} c_n c_m \langle \psi_n | \psi_m \rangle} \\ &= \frac{\sum_n |c_n|^2 E_n}{\sum_n |c_n|^2} = \frac{|c_0|^2 E_0}{|c_0|^2} + \frac{\sum_{n>0} |c_n|^2 E_n}{\sum_{n>0} |c_n|^2} \\ &= E_0 + \frac{\sum_{n>0} |c_n|^2 E_n}{\sum_{n>0} |c_n|^2} \geq E_0 \end{aligned} \quad (2.10)$$

### 2.4.2 Hohenberg-Kohn Theorems

This theorem states that the (non-degenerate) ground state density  $n_0(\mathbf{r})$  uniquely determines the external potential  $V_{ext}(\mathbf{r})$  up to an additive constant. [32]

Assuming that another potential  $V'_{ext}(\mathbf{r})$  with ground state wave function  $\psi'_0$  corresponds to the same density  $n_0(\mathbf{r})$ , the ground state energies would be  $E_0 = \langle \psi_0 | \hat{\mathbf{H}} | \psi_0 \rangle$  and  $E'_0 = \langle \psi'_0 | \hat{\mathbf{H}}' | \psi'_0 \rangle$  where  $\hat{\mathbf{H}} = \hat{\mathbf{F}} + \hat{\mathbf{V}}_{ext}$  and  $\hat{\mathbf{H}}' = \hat{\mathbf{F}} + \hat{\mathbf{V}}'_{ext}$ . Applying the vari-

ational principle by using  $\psi'_0$  as a trial wave function:

$$\begin{aligned}
E_0 &< \langle \psi'_0 | \hat{\mathbf{H}} | \psi'_0 \rangle = \langle \psi'_0 | \left( \hat{\mathbf{H}} - \hat{\mathbf{H}}' + \hat{\mathbf{H}}' \right) | \psi'_0 \rangle \\
&= \langle \psi'_0 | \hat{\mathbf{H}}' | \psi'_0 \rangle + \langle \psi'_0 | \left( \hat{\mathbf{V}}_{ext} - \hat{\mathbf{V}}'_{ext} \right) | \psi'_0 \rangle \\
&= E'_0 + \langle \psi'_0 | \left( \hat{\mathbf{V}}_{ext} - \hat{\mathbf{V}}'_{ext} \right) | \psi'_0 \rangle
\end{aligned} \tag{2.11}$$

Similarly, taking  $\psi_0$  as a trial wave function:

$$\begin{aligned}
E'_0 &< \langle \psi_0 | \hat{\mathbf{H}}' | \psi_0 \rangle = \langle \psi_0 | \left( \hat{\mathbf{H}}' - \hat{\mathbf{H}} + \hat{\mathbf{H}} \right) | \psi_0 \rangle \\
&= E_0 - \langle \psi_0 | \left( \hat{\mathbf{V}}_{ext} - \hat{\mathbf{V}}'_{ext} \right) | \psi_0 \rangle
\end{aligned} \tag{2.12}$$

Summing the left and right hand sides of equations 2.11 and 2.12, one obtains the contradictory result:

$$E_0 + E'_0 < E'_0 + E_0 \tag{2.13}$$

Hence the theorem is proven by *reductio ad absurdum*.

The second theorem states that the ground state energy is a functional of the ground state density.

## 2.5 Kohn-Sham Equations

In order to be able to use Hohenberg–Kohn theorems in practice for real calculations, Kohn and Sham [39] provided a way in which the density is written in terms of fictitious single particle orbitals:

$$n(\mathbf{r}) = \sum_i^N |\phi_i(\mathbf{r})| \tag{2.14}$$

$$E[n(\mathbf{r})] = \sum_i^N \epsilon_i \tag{2.15}$$

In essence, Kohn–Sham formalism assumes an auxiliary system of non-interacting electrons experiencing an effective potential,  $V_{eff}$ , which mimics not only the ionic potentials but the interactions with all other electrons as well.  $V_{eff}$  contains both the external potential and electron–electron interaction contributions. The latter is broken into two parts: the Hartree term describing the Coulombic repulsion for a

non-interacting electron system, plus, the exchange–correlation potential,  $V_{xc}$ , for the effects arising from the interaction among electrons. Then  $V_{eff}$  in terms of density is:

$$V_{eff} = \int V_{ext}(\mathbf{r})n(\mathbf{r})d\mathbf{r} + \int \frac{n(\mathbf{r})n(\mathbf{r}')}{|\mathbf{r} - \mathbf{r}'|}d\mathbf{r}d\mathbf{r}' + V_{xc} . \quad (2.16)$$

These definitions of the density and the effective potential leads to single-particle Schrödinger like equations:

$$\hat{\mathbf{H}}_{eff} = \left[ \hat{\mathbf{T}}' + \hat{\mathbf{V}}_{eff} \right] \Phi_i(\mathbf{r}) = \epsilon_i \Phi_i(\mathbf{r}) . \quad (2.17)$$

The kinetic energy,  $\hat{\mathbf{T}}'$ , in the Kohn–Sham Hamiltonian  $\mathbf{H}_{eff}$ , is denoted by a prime as it is no longer the kinetic energy of the real system. A kinetic energy correction for the interacting case is included inside  $V_{xc}$ .

The Kohn–Sham equations has the peculiar characteristic that the  $V_{eff}$  depends on the density which already is the unknown parameter to be found. Eventually, they can only be solved by iterative calculations forming a self-consistent cycle, explained further in Section 2.6.

### 2.5.1 Exchange–Correlation Functionals

The exchange–correlation effects are due to the Pauli exclusion principle. The overlap of the anti-symmetric wave functions of interacting electrons results in an attractive or a repulsive effect apart from Coulombic forces. The complicated nature of the exchange–correlation energy  $E_{xc}$  prevents it to be expressible analytically in terms of the density. Thus, it is an approximated functional available in several different types each of which may work better in different systems. The most commonly used functionals are Local Density Approximation (LDA) and Generalized Gradient Approximation (GGA). Given  $E_{xc}$ , the corresponding potential  $V_{xc}$  used in Kohn–Sham equations is found by taking its functional derivative.

In constructing LDA functionals, it is assumed that locally, the density is homogeneous and the total exchange–correlation energy can be found by integrating the cor-

responding exchange–correlation energies:

$$E_{xc}^{LDA} = \int n(\mathbf{r})\epsilon_{xc}^{hom}(n(\mathbf{r}))d\mathbf{r} . \quad (2.18)$$

The homogeneous, local exchange–correlation energy,  $\epsilon_{xc}^{hom}$ , is obtained by adding the separately found exchange and correlation parts. The exchange and correlation energies are complicated as they are related to the whole system rather than pairwise interactions. Their determination is made by Quantum Monte Carlo simulations using different parameters. LDA types differ in this parametrization process and some of the most commonly used types are Perdew–Zunger (PZ),Perdew–Wang (PW).

GGA functionals attempt to improve LDA approach by including the gradient of the density in the integration:

$$E_{xc}^{GGA} = \int n(\mathbf{r})\epsilon_{xc}[n(\mathbf{r}), \nabla n(\mathbf{r})]d\mathbf{r} . \quad (2.19)$$

Most common GGA types are Becke–Lee–Yang–Parr (BLYP) and Perdew–Burke–Ernzerhof (PBE). Although GGA not necessarily improves LDA it was proved to be more accurate in highly inhomogeneous systems.

### 2.5.2 Plane Wave Expansion

To be able to numerically solve the Kohn–Sham equations, the Kohn–Sham orbitals  $\Phi_i(\mathbf{r})$  should be expanded in terms of a finite basis set. The basis can be chosen as consisting of plane waves or localized orbitals. Localized orbitals are more appropriate in small, isolated systems such as atoms, molecules and nanoclusters. In this thesis, we performed all the calculations using the PWSCF software which employs plane waves.

Using a plane wave basis requires working in the reciprocal space. The relation between the real space primitive vectors  $\mathbf{a}$  and the primitive reciprocal space vectors  $\mathbf{b}$  is:

$$\mathbf{a}_i \cdot \mathbf{b}_j = 2\pi\delta_{ij} . \quad (2.20)$$

The reciprocal unit cell defined by  $\mathbf{b}$  is the first Brillouin zone and the infinitely many vectors lying in this volume are denoted by  $\mathbf{k}$ . The vectors  $\mathbf{G}$  spanning the whole reciprocal space are defined as:

$$\mathbf{G}_m = m_i \mathbf{b}_i \quad (2.21)$$

where  $m$  is an integer.

Plane wave expansion of the Kohn–Sham orbitals is a direct result of the crystal structure. In a crystal as the ions are arranged regularly, the potential created by this system is periodic. According to Bloch’s Theorem [21], the wavefunction of particles placed in this potential will also be periodic with the same periodicity as the potential. It states that the eigenfunctions  $\Phi(\mathbf{r})$  of the Schrödinger equation for such a potential is the product of a cell-periodic function,  $u(\mathbf{r}, \mathbf{k})$  and a plane wave :

$$\Phi(\mathbf{r}) = u(\mathbf{r}, \mathbf{k}) \cdot e^{i\mathbf{k}\cdot\mathbf{r}} . \quad (2.22)$$

As any periodic function can be expanded in terms of plane waves,  $u(\mathbf{r}, \mathbf{k})$  can be written as:

$$u(\mathbf{r}, \mathbf{k}) = \frac{1}{\sqrt{\Omega}} \sum_{\mathbf{G}_m} c_i(\mathbf{k}, \mathbf{G}_m) e^{\mathbf{G}_m \cdot \mathbf{r}} \quad (2.23)$$

where  $\Omega$  is the volume of the unit cell and  $c_i(\mathbf{k}, \mathbf{G}_m)$  are the complex expansion coefficients.

Then the wavefunction of the system expanded in terms of plane waves is:

$$\begin{aligned} \Phi(\mathbf{r}) = \Phi_i(\mathbf{r}, \mathbf{k}) &= \frac{1}{\sqrt{\Omega}} \sum_{\mathbf{G}_m} c_i(\mathbf{k}, \mathbf{G}_m) e^{i(\mathbf{k}+\mathbf{G}_m)\cdot\mathbf{r}} \\ &= \sum_{\mathbf{G}_m} c_i(\mathbf{k}, \mathbf{G}_m) |\mathbf{k} + \mathbf{G}_m \rangle \end{aligned} \quad (2.24)$$

For a given  $\mathbf{k}$ , the orthonormality property of the plane waves reads as:

$$\langle \mathbf{k} + \mathbf{G}_{m'} | \mathbf{k} + \mathbf{G}_m \rangle = \delta_{mm'} . \quad (2.25)$$



Then the he Kohn–Sham Hamiltonian can be written as:

$$\sum_{\mathbf{G}_m} \langle \mathbf{k} + \mathbf{G}_{m'} | \hat{\mathbf{H}}_{eff} | \mathbf{k} + \mathbf{G}_m \rangle c_i(\mathbf{k}, \mathbf{G}_m) = \epsilon_i \sum_{\mathbf{G}_m} \delta_{mm'} c_i(\mathbf{k}, \mathbf{G}_m) = \epsilon_i \sum_{\mathbf{G}_m} c_i(\mathbf{k}, \mathbf{G}_{m'}) . \quad (2.26)$$

This matrix equation can be written compactly as:

$$\sum_{\mathbf{G}_m} H_{mm'} c_{i,m} = \epsilon_i \sum_{\mathbf{G}_m} c_{i,m'} . \quad (2.27)$$

Each operator forming the Hamiltonian should be considered separately. The kinetic energy operator is given by:

$$\langle \mathbf{k} + \mathbf{G}_{m'} | \hat{\mathbf{T}} | \mathbf{k} + \mathbf{G}_m \rangle = - \langle \mathbf{k} + \mathbf{G}_{m'} | \frac{1}{2} \nabla^2 | \mathbf{k} + \mathbf{G}_m \rangle = \frac{1}{2} |\mathbf{k} + \mathbf{G}_m|^2 \delta_{mm'} . \quad (2.28)$$

The effective potential is periodic as stated before and it can be expanded as the wave function actually is an inverse Fourier transformation:

$$V_{eff}(\mathbf{r}) = \frac{1}{\sqrt{\Omega}} \sum_{\mathbf{G}_m} V_{eff}(\mathbf{G}_m) e^{i(\mathbf{k} + \mathbf{G}_m) \cdot \mathbf{r}} . \quad (2.29)$$

The Fourier transformation from real to reciprocal space integrated over real space vectors is:

$$V_{eff}(\mathbf{G}) = \frac{1}{\sqrt{\Omega}} \int_{\mathbf{r}} V_{eff}(\mathbf{r}) e^{-i(\mathbf{k} + \mathbf{G}_m) \cdot \mathbf{r}} . \quad (2.30)$$

The effective potential matrix is given as:

$$\langle \mathbf{k} + \mathbf{G}_{m'} | V_{eff}(r) | \mathbf{k} + \mathbf{G}_m \rangle = \sum_{\mathbf{G}_m} V_{eff}(\mathbf{G}_m) \delta_{\mathbf{G}_m - \mathbf{G}'_m, \mathbf{G}_m} = V_{eff}(\mathbf{G}_m - \mathbf{G}_{m'}) . \quad (2.31)$$

Then the matrix elements of the Kohn–Sham Hamiltonian:

$$H_{mm'} = \frac{1}{2}|\mathbf{k} + \mathbf{G}_m|^2\delta_{mm'} + V_{eff}(\mathbf{G}_m - \mathbf{G}_{m'}) . \quad (2.32)$$

The expansions requires summation over the infinitely many  $\mathbf{G}$ -vectors which is a computationally impossible task. However, for large  $\mathbf{G}$ , plane waves become negligible, thus the sum can be truncated at a certain value. This value is called the cut-off radius,  $E_{cut}$ , usually expressed in terms of kinetic energy in units of electronvolts or Rydbergs. Larger  $E_{cut}$  results in more accurate results but takes more computational time as the number of plane waves will increase accordingly. In order to determine the smallest possible  $E_{cut}$  value that gives accurate results, convergence tests should be conducted over a range of values.

Another approximation is the discretisation of the k-points set. Depending on the fact that the wavefunctions at the k-points that are very close to each other are almost identical, a certain region in the reciprocal space can be represented by a single k-point. Naturally, the denser the discrete k-points set is, the more accurate (but slower) the calculations will be. Different methods for the discretisation have been proposed and in this thesis we used the Monkhorst–Pack scheme [50]. Similar to the determination process of  $E_{cut}$ , the k-points grid should be subjected to convergence tests.

Lastly, as periodicity is essential for the plane wave basis, calculations are made over infinitely many periodic images of the considered unit cell extending in three dimensions even if the system does not have three dimensional periodicity. Thus, in performing plane wave calculations for finite systems, such a system should be placed inside a large enough supercell preventing the interaction between the periodic images.

### 2.5.3 Pseudopotentials

Around regions close to the ions, the potential and hence the electronic wave function has a highly oscillating behaviour. Accurate representation of such a behaviour requires a very large number of plane waves. The oscillations are mainly due to the core

electrons and the part of the wave functions of the valence electrons around the ions oscillate as well due to orthogonality condition. After a certain radius, the wave function whose behaviour is determined by the valence electrons tend to become smooth which can be appropriately described by a few plane waves. Owing to the fact that almost any chemical and physical property of materials depends on the behavior of the valence electrons, the oscillatory core part is replaced by smoother pseudopotentials and as a result only the density of the valence electrons is considered in DFT calculations.

#### 2.5.4 Pseudopotential Generation

A pseudopotential generated for an atom should obey certain criteria in order to be accurate and transferable:

1. The pseudo wave function should overlap with the real wave function beyond a certain core radius,  $r_c$ .
2. The eigenvalues for a reference atomic configuration of the real and pseudo wave functions of the valence electrons should match.
3. The logarithmic derivatives of the real and pseudo wave functions should be equal at  $r_c$ .

A fourth criterion, called the norm-conservation condition [30] can also be counted which requires that the integrated charge inside  $r_c$  for the real and pseudo wave functions should agree. However this condition can be relaxed for the sake of obtaining smoother, hence computationally faster pseudopotentials. A widely employed class of pseudopotentials abandoning norm-conservation are ultrasoft pseudopotentials. In our calculations we used Vanderbilt type ultrasoft pseudopotentials [?] for each atom.

In this thesis, other than the well-known Perdew-Zunger (PZ)-LDA functionals and Perdew-Burke-Erzenhof (PBE)-GGA functionals, revised PBE (revPBE) and c09x functionals which were shown to work well along with van-der Waals corrections which are explained in Section 2.7. The GGA functional in equation 2.5.1 can also

be expressed as:

$$E_{xc}^{GGA} = \int n(\mathbf{r}) \epsilon_{xc} n(\mathbf{r}) F_x(s) d\mathbf{r} . \quad (2.33)$$

where  $F_x(s)$  is called the enhancement factor depending on the dimensionless density gradient  $s$  with  $s = \frac{|\nabla n|}{2k_F n}$ . The PBE and revPBE enhancement factors are:

$$F_x(s) = 1 + \frac{\mu s^2}{1 + \mu s^2 / \kappa} \quad (2.34)$$

and for the c09x exchange functional it is:

$$F_x(s) = 1 + \mu s^2 e^{-\alpha s^2} + \kappa (1 - e^{-\alpha s^2 / 2}) \quad (2.35)$$

Pseudopotentials with revPBE and c09x exchange parts were generated in order to use in combination with corresponding van-der Waals functionals. The all-electron and pseudopotential wave-functions of the pseudopotential generation for Carbon atom are presented in Figure 2.1.

## 2.6 Self-Consistency Cycle

The iterative cycle needed to solve the Kohn–Sham equations is constructed as follows: starting from an initially guessed input density,  $n_{in}$ , the effective potential  $V_{eff}$  is calculated and fed to the Kohn–Sham equations. The Kohn–Sham Hamiltonian is solved with this  $V_{eff}$  and the calculated new output density,  $n_{out}$ , is compared to  $n_{in}$ . If they are not consistent, the cycle repeats itself until self-consistency is achieved.

Rather than starting from a guessed density at the beginning of each cycle or directly feeding in the calculated output density, a mixture of the input and output densities is preferred for easier convergence. The simplest method is linear mixing formulated as:

$$n_{in}^{i+1} = \beta n_{out}^i + (1 - \beta) n_{in}^i = n_{in}^i + \beta (n_{out}^i - n_{in}^i) \quad (2.36)$$

where  $i$  denotes the  $i^{th}$  cycle and  $\beta$  is a number between 0 and 1. Different mixing schemes providing faster convergence have been proposed. A commonly used scheme is Broyden mixing [11] which we used for the bulk calculations in this thesis.

Most of the computational effort in the self-consistent cycle is spent to the solution of the Kohn–Sham equations expanded in a plane wave basis. The calculations re-

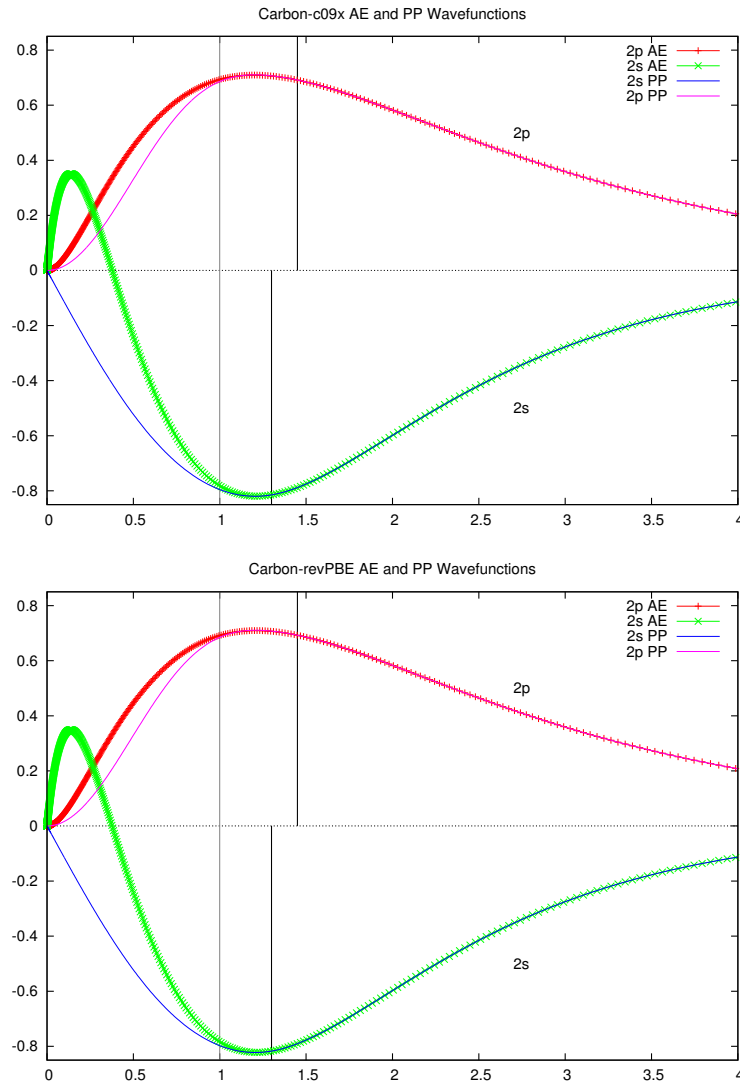


Figure 2.1: All electron and pseudopotential wave functions for the c09x and revpbe functionals.

quire diagonalisation of very large matrices which makes direct diagonalisation too expensive. Different algorithms have been proposed for faster diagonalisation. In this thesis we used the Davidson algorithm [18].

## 2.7 van-der Waals Interaction

As the standard DFT functionals are either local (LDA) or semi-local (GGA), hence only good for modelling short-range electronic correlations; the weak, long-ranged

van der Waals forces cannot be described. In recent years it became possible to include the van-der Waals effects by directly adding a semi-empirical dispersion correction to the total energy as in the DFT-D method [27, 28] or by reconstructing the exchange-correlation functional (called the vdW-DF method [20]) which allows a self-consistent treatment.

In density functional theory, the standard energy functional is given as,

$$E_{DFT}[n] = T[n] + V_{ee}[n] + V_{ion}[n] + E_{xc}[n] \quad (2.37)$$

Within DFT-D, the energy functional is improved by simply adding a semi-empirical dispersion term  $E_{disp}$ :

$$E_{DFT-D} = E_{DFT} + E_{disp} \quad (2.38)$$

The dispersion correction describes the London forces resulting from the instantaneously induced dipoles due to the fluctuation of electron densities as  $\frac{C_6}{R^6}$  with  $R$  being the interatomic distance and  $C_6$  being the semi-empirical coefficient proportional to ionization potentials and dipole polarizabilities. In more detail,  $E_{disp}$  is given for periodic boundary conditions as [3]:

$$E_{disp} = -\frac{1}{2} \sum_{i,j} C_{6ij} \left[ \sum_{\mathbf{R}} f_{damp} \frac{1}{|\mathbf{r}_{ij} + \mathbf{R}|^6} \right] \quad (2.39)$$

and the damping function to avoid singularities for small  $R$  is:

$$f_{damp} = s_6 \times \frac{1}{1 + \exp \left[ -d \times \left( \frac{|\mathbf{r}_{ij} + \mathbf{R}|}{r_0} - 1 \right) \right]} \quad (2.40)$$

where  $s_6$  is a scaling factor which depends on the exchange-correlation functional, the parameter  $d$  tunes the steepness of the function.

In the vdW-DF method, the exchange-correlation  $E_{xc}$  is given as

$$E_{xc} = E_x^{GGA} + E_c^{LDA} + E_c^{nl} \quad (2.41)$$

where the exchange energy ( $E_x^{GGA}$ ) is evaluated within GGA, the local part of the correlation ( $E_c^{LDA}$ ) is approximated in LDA and a non-local correlation contribution ( $E_c^{nl}$ ) is included to describe dispersive interactions.

The van-der Waals forces at one point of the system depend on the variations in the charge density at another point. Thus the non-local part of the exchange-correlation energy is given as a double-space integral:

$$E_c^{nl}[n] = \frac{1}{2} \int \int d\mathbf{r} d\mathbf{r}' n(\mathbf{r}) n(\mathbf{r}') \Phi(\mathbf{r}, \mathbf{r}') \quad (2.42)$$

where the interaction kernel  $\Phi(\mathbf{r}, \mathbf{r}')$  depends on  $\mathbf{r} - \mathbf{r}'$  and the charge densities  $n(\mathbf{r})$ ,  $n(\mathbf{r}')$  and their gradients at  $\mathbf{r}$  and  $\mathbf{r}'$ . The vdW-DF2 method uses a large-N asymptotic expansion in the evaluation of the kernel which improves the accuracy of vdW-DF for various systems [44].

Although the vdW-DF and vdW-DF2 methods allow a self-consistent treatment from scratch, they can also be included as a post-GGA perturbation over the charge densities calculated with usual semi-local functionals. Some studies suggest that following the latter method has immaterial consequences, however, other studies claim that fully self-consistency is necessary for certain systems. vdW-DF and vdW-DF2 methods are implemented in Quantum Espresso through an efficient algorithm proposed by Roman-Perez and Soler [59] and the computational load required for a self-consistent treatment does not significantly vary from standard calculations. Due to this the fully self-consistency way was adopted through this thesis.

It is known that the type of the GGA exchange employed in vdW calculations may significantly affect certain properties of a system such as interaction distances, binding energies etc. [43]. The revPBE exchange is typically used in combination with the vdW-DF method as it shows little of the spurious bonding effect observed in many other GGA flavors [42]. However, revPBE is too repulsive at short distances and the c09 exchange was proposed as a remedy to this shortcoming [15]. Despite this correction, the c09 exchange used in combination with vdW-DF can overestimate the

binding energies which is mostly due to the vdW-DF itself. In the vdW-DF2 method, originally the rPW86 functional was used. Many other flavours, such as hybrid functionals can also be employed. There is still not a universal convention about the best suited functional to combine with the vdW-DF methods and in this study the most abundantly used functionals are considered. There also doesn't exist much information in the literature about the effects of matching the flavour of the pseudopotentials with the exchange functionals. Here, matching pairs are used and revPBE and c09 pseudopotentials were generated as explained in 2.5.4.

### 2.7.1 Benchmarking vdW functionals

To decide on the van-der Waals functional to use in the calculations, benchmark tests involving graphite and bilayer graphene were conducted. Graphite and bilayer graphene consist of graphene layers held together with van-der Waals forces. The most common naturally occurring form for graphite is the ABA (Bernal) stacking, whereas bilayer graphene has AA stacking. The in-plane lattice parameters are identical to graphene and the interlayer separation is about 3.3 Å for both structures. The vertical lattice parameters and exfoliation energies were calculated for graphite and bilayer graphene by fixing the in-plane lattice parameter to the optimized values of graphene which are given Table 2.1.

Table 2.1: Optimized lattice constants for graphene with different functionals

Functional	$a[\text{Å}]$	% error
LDA	2.440	0.81
GGA	2.463	0.12
vdW-DF <sup>revPBE</sup>	2.481	0.85
vdW-DF2 <sup>c09</sup>	2.464	0.16
<i>Exp.</i>	2.461	

The exfoliation energy for graphite was calculated from the formula:

$$E_{ex} = E_{graphite} - (3 \times E_{graphene}) \quad (2.43)$$



and for bilayer graphene:

$$E_{ex} = E_{bilayer} - (2 \times E_{graphene}) \quad (2.44)$$

Table 2.2: Binding energies and distances for graphite calculated with different functionals.

Functional	$d[\text{\AA}]$	$E_b(\text{meV/})$
LDA	3.38	-24
GGA	4.29	-3
vdW-DF <sup>revPBE</sup>	3.75	-54
vdW-DF2 <sup>c09</sup>	3.38	-54
<i>Exp.</i>	3.34	-52±5

Through these tests, it was decided that the vdW-DF2<sup>c09</sup> yields the best results for graphene-based structures, hence this flavor was employed in the calculations involving van-der Waals interactions. These benchmark tests are also in good agreement with previous studies [29].

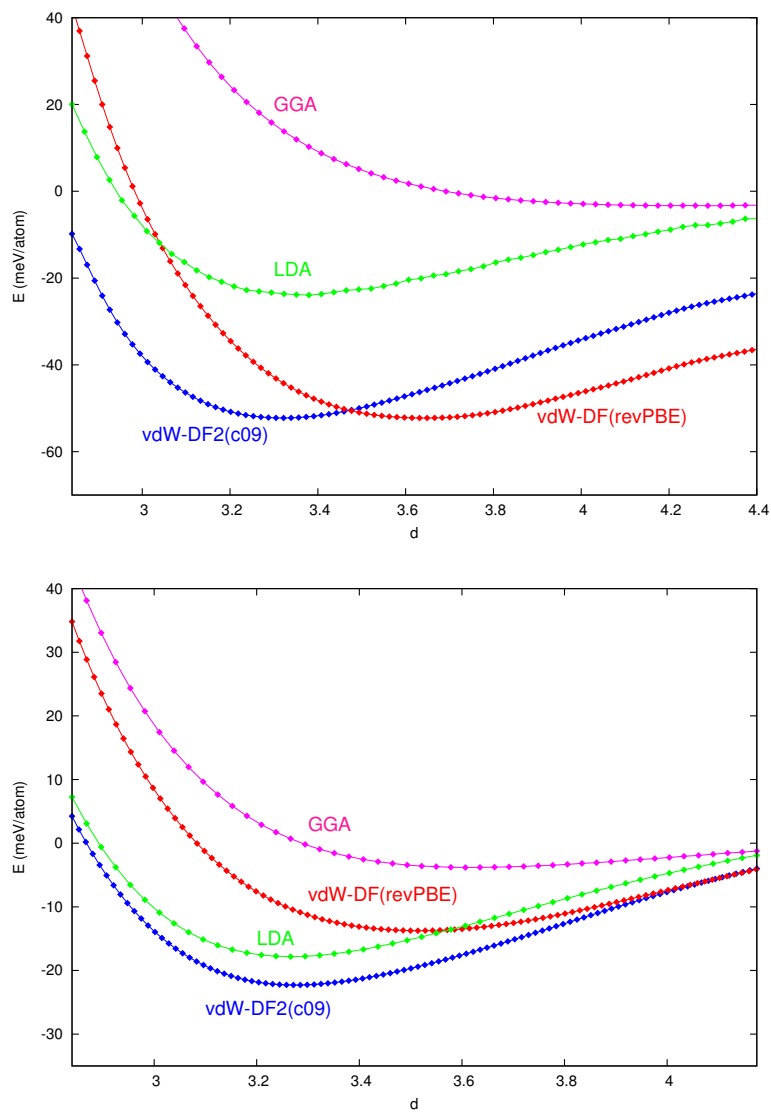


Figure 2.2: The binding energy difference plots for different functionals for graphite(a) and bilayer graphene(b).

## CHAPTER 3

### CARBON NANOTUBES ON GRAPHENE ON METALS

In this chapter, we study the geometry, energetics and electronic structure of single walled carbon nanotubes adsorbed on isolated graphene, the graphene/Cu(111) and graphene/Ni(111) interfaces and carbon nanotubes on graphene supported by the Cu(111) surface.

#### 3.1 Computational Details

Four different exchange-correlation functionals (and corresponding pseudopotentials) including both standard and van-der Waals types are employed: (i) local density approximation (LDA) with Perdew-Zunger (PZ) parametrization [85], (ii) generalized gradient approximation (GGA) with Perdew-Burke-Erzenhof (PBE) parametrization [55], (iii) vdW-DF [20] with revised PBE [82] exchange (vdW-DF<sup>revPBE</sup>), (iv) vdW-DF2 [44] with c09 [15] exchange (vdW-DF2<sup>c09</sup>). All the pseudopotentials involved are of the Vanderbilt ultrasoft type [71]. The generation of the c09x and revPBE pseudopotentials are explained in Chapter 2. We account for the dispersive interactions by employing Van-der Waals density functionals fully self-consistently at the vdW-DF2 [44] level. The necessity to use different functionals are explained throughout the section.

We used 1x6x1 and 6x6x1 Monkhorst-Pack [50] grids for k-points sampling of the CNT/graphene and CNT/metal calculations respectively. A kinetic energy cut-off of 35 Ryd gave well converged results for all systems and a Marzari-Vanderbilt smearing [49] with a broadening of 0.02 Ryd was present in the calculations involving metals.

The unit cell for the adsorption of a horizontally aligned CNT on an isolated graphene sheet consists of a rectangular strip of graphene placed underneath the CNT. We considered the interaction of graphene with CNT(6,0) and CNT(8,0) nanotubes. The CNT-CNT distance between periodic images and the vacuum region in the vertical direction were larger than 10Å in all cases to prevent interactions. The  $>10\text{\AA}$  constraint between parallel CNTs is satisfied by basically using the unrolled version of the CNT as the graphene sheet in the unit cell, i.e. and an  $n \times 1$  graphene sheet is used for a CNT( $n,0$ ).

From the binding energy versus separation curves plotted for different functionals for a (8,0) CNT on a graphene layer in the directly-on-top geometry that is presented in Figure 3.1, it is evident that van-der Waals functionals should be used as GGA cannot yield any binding at all. Even though LDA may be used to accurately model weak interactions (ref), the underestimation of the lattice parameters as seen in Table 2.1 can mimic strain on the structures which is known to affect the electronic structure (ref). The vdw-DF2-c09 functional was preferred as it gave accurate results in the benchmark tests for graphite and bilayer graphene as presented in Section 2.8. In these calculations the graphene layer was fixed and the energies were calculated self-consistently by scanning over the vertical distance. The separation  $l$  is taken perpendicularly from the bottom of the CNT to the graphene layer. The binding energy is defined as:

$$E_b = E(l) - E(l \rightarrow \infty) \quad (3.1)$$

where  $E(l)$  is the calculated total energy and  $E(l \rightarrow \infty)$  is the total energy of the non-interacting system.

For the graphene/metal calculations, graphene was put on top of 5 layers of metal whose last layer was kept fixed during geometric optimization. In the CNT+graphene+metal calculations, 3 layers of Cu was considered.

### 3.2 CNTs on Graphene

In searching for stable adsorption geometries and the corresponding interaction distances for the CNT on the graphene sheet we started with the parallel, directly-on-top

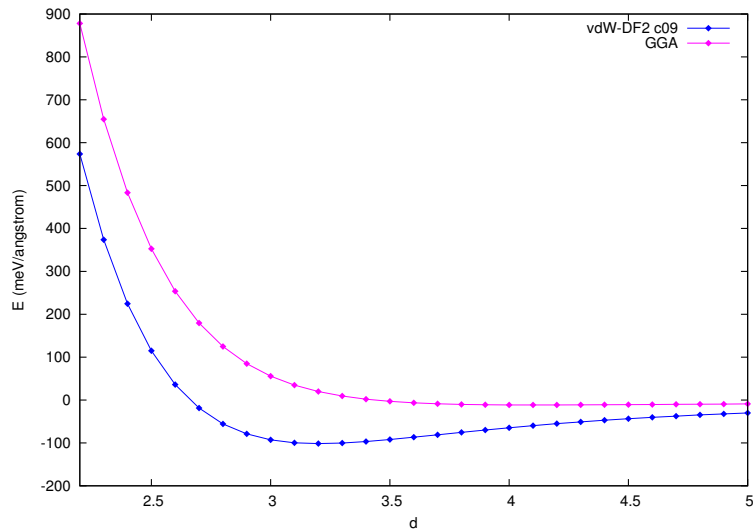


Figure 3.1: The binding energy vs. distance plots for a horizontally aligned (8,0) CNT on graphene calculated with PBE-GGA and vdW-DF2<sup>c09</sup> functionals.

configuration and scanned over various other sites by rolling the CNTs along the central axis and/or by shifting in the horizontal direction. Within this constraint, basically two distinct alignments exist noted as directly-on-top and shifted geometries as shown in Figure 3.2. Any axial rotation or horizontal shift corresponds to a site in between these two configurations. The directly-on-top geometry is an analogue to the AA stacking of bilayer graphene. Cross-registries (twisted geometries) were not considered as they require much larger unit cells.

We have found two different stable adsorption modes for the horizontally aligned (6,0) and (8,0) CNTs on graphene. One is physisorption in which the nanotubes atabilizes at about 3 Å above the graphene layer. Another stable adsorption phase of a CNT on a graphene sheet is meditated through the formation of single or double C-C bonds. Allowing the system to fully relax starting from a small initial separation (<2Å) results in deformed nanotubes bonded to graphene where a cusp forms at the bonding site. In the directly on top geometry, the CNT is bonded to the graphene layer with a single C-C bond per unit cell. A double C-C bond which occurs when the CNT is slightly rotated. All these three cases are seen in Figure 3.3. In the shifted geometry, C-C bond formation did *not* occur and the CNT remained weakly interacting regardless of the initial separation.

We defined the binding energy per length and calculated it by subtracting the energies of the deformed CNT and graphene layer from the total energy of the system and divide it by the length of the unit cell in y-direction. The equilibrium bond lengths and the binding energies per length calculated with the vdW-DF2<sup>c09</sup> functional are summarized in Table 3.1. Physisorption yielded rather weak binding energies per length which are 11 meV and 9 meV for the (6,0) and (8,0) CNTs respectively. The C–C bond lengths are about 1.6 Å whenever they are formed. The binding energies in all cases are slightly larger for the CNT (6,0).

The CNT(6,0) is metallic whereas the (8,0) CNT is a small-gap semiconductor with a band gap of about 0.5 eV. The density of states(DOS) of the (8,0) CNT adsorbed on graphene via van-der Waals forces, a single C-C bond and a double C-C bond are seen Figure 3.3. The DOS of the isolated graphene layer and the isolated CNT are plotted along. The zero of the plot coincides with the Fermi level of graphene. As seen from the zoomed plots around the Fermi level, the total CNT+graphene system seems to be remained semiconducting whereas the C-C bonds rendered the system metallic.

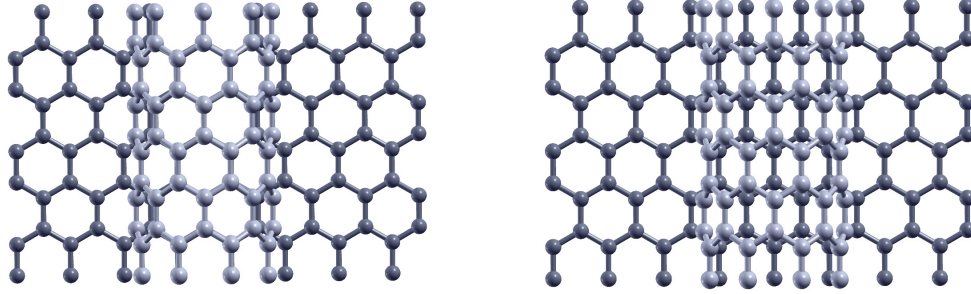


Figure 3.2: The on-top (left) and shifted (right) geometries of a CNT on graphene.

Table 3.1: The equilibrium bond lengths and the binding energy per length for the adsorption of CNT(6,0) and CNT(8,0) on graphene through van-der Waals, single and double C-C bonds.

		$b_{eq}[\text{\AA}]$	$E_b/l[\text{meV}/\text{\AA}]$
CNT(6,0)	VdW	3.14	11
	Single C-C	1.62	62
	Double C-C	1.60	34
CNT(8,0)	VdW	3.24	9
	Single C-C	1.62	52
	Double C-C	1.60	31

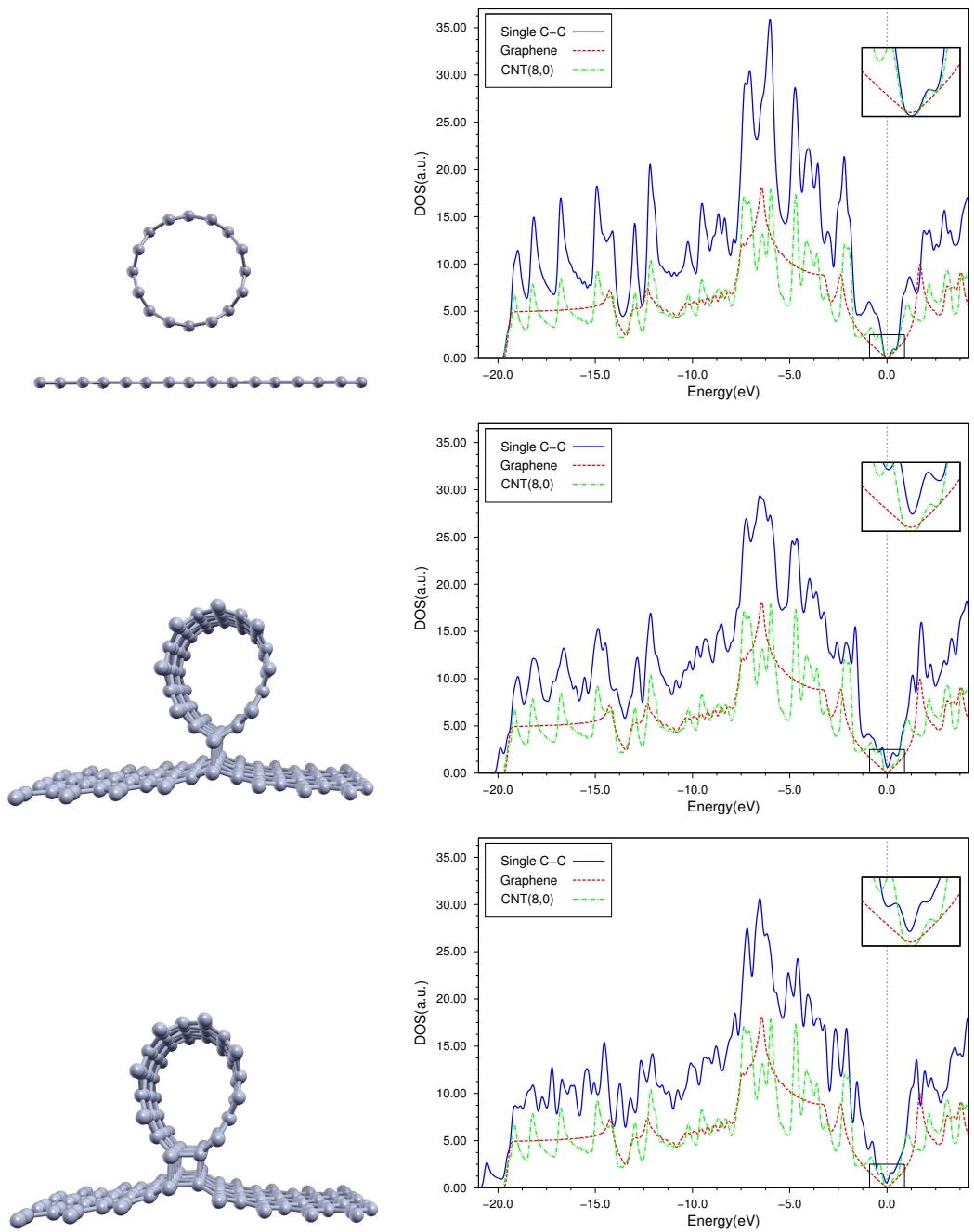


Figure 3.3: The optimized structures and density of states plots for a CNT(8,0) on graphene for van-der Waals interaction (a), single C-C bonds (b) and double C-C bonds (c).



### 3.3 Graphene/Metal Interface

Graphene adsorbs to metals with a small lattice mismatch in a planar geometry without corrugations and generally has a single most stable adsorption configuration. These metals have a face-centered cubic (FCC) structure and they are divided into two classes with respect to the interaction strength: graphene weakly interacts with Cu, Al, Ag and Au, while it strongly interacts with Ni, Co and Pd.

In order to work with periodic boundary conditions in plane-wave DFT studies, a single lattice parameter should be adopted. The lattice constant of graphene can be fixed to that of the metals or the lattice parameter of metals can be fixed to that of graphene. Although the lattice mismatches are small, it was shown that these two cases may lead to significant differences such as varying type and amount of doping of the graphene layer [66]. Adopting the lattice constant of metals models processes in which graphene is grown on or transferred to metallic surfaces. Fixing lattice constants to graphene corresponds to depositing metals onto the graphene layer. Most applications involve processes as represented by the first model, however the significant underestimation or overestimation of the lattice parameters of the metals with certain functionals may lead to unrealistic results in DFT calculations. As a result some studies employ experimental values for the lattice constants of the metals [78]. The surface lattice parameter  $\alpha_{surface}$  of the (111) surface of an FCC metal is calculated from the bulk lattice parameter  $a_{lat}$  from the relation:

$$\alpha_{surface} = a_{lat} \times \frac{\sqrt{2}}{2} = \frac{a_{lat}}{\sqrt{2}} \quad (3.2)$$

In this section, we investigate Graphene/Cu(111) and graphene/Ni(111) interfaces as Ni and Cu are representative metals from both weak and strong interaction classes, the lattice mismatches are relatively small and also, they are both important in electronic applications and epitaxial growth of graphene. Both experimental and theoretical studies suggest that the most stable adsorption geometry of graphene on Ni(111) is the top-fcc configuration where C atoms are alternately positioned over the metal atoms of the first and third layers as seen Figure 3.4. Although experimental evidence is lacking for Cu, theoretical calculations predict the same configuration for Cu(111).

Apart from the lattice constant, the graphene–metal interface is also very sensitive to

the type of the functional. LDA calculations divide the metals in two classes where graphene is either chemisorbed or physisorbed which is in-line with experimental results [25]. GGA predicts the lattice parameters better than LDA, but fails to produce accurate values for the binding energies and distances. It either gives too weak binding or no binding at all. It was shown that VdW-DF<sup>revpbe</sup> gives similar results to GGA [72] while VDW-DF2<sup>c09</sup> is well suited and it gives both the adsorption distances and energies in good agreement with experiments. [29]. VDW-DF2<sup>c09</sup> also produces the lattice constants close to the experimental values. The lattice constants for Cu and Ni calculated with different functionals are listed in Table 3.2.

Table 3.2: Experimental bulk lattice constants, surface lattice constants and surface-graphene percent mismatches calculated with different functionals for Cu and Ni.

	Func.	$a(\text{\AA})$	$\alpha_{surf}(\text{\AA})$	% mismatch
Cu	LDA	3.55	2.51	2.89
	GGA	3.67	2.60	5.56
	vdW <sup>revPBE</sup>	3.71	2.62	5.60
	vdW2 <sup>c09</sup>	3.59	2.54	3.08
	<i>Exp.</i>	3.61	2.55	3.66
Ni	LDA	3.43	2.43	0.41
	GGA	3.52	2.49	1.09
	vdW <sup>revPBE</sup>	3.56	2.52	1.57
	vdW2 <sup>c09</sup>	3.47	2.45	0.58
	<i>Exp.</i>	3.52	2.49	1.18

The band structure of graphene adsorbed on the Ni(111) surface calculated with L(S)DA is shown in Figure 3.4. Graphene is chemisorbed on Ni and graphene states hybridizes with the d states of Ni which results in the opening of a gap at  $\mathbf{K}$  in accordance with previous studies. For the Cu(111) surface, two rather different results were obtained by using two different lattice parameters. As the whole system is fixed to lattice constant of the metal, the band structure displays n-doping as predicted by previous studies, while the graphene-metal separation was found to be 2.54 Å which is significantly shorter than the experimental and theoretical data which suggests a distance of 3.3 Å. On the other hand, as the system is calculated by fixing the lattice constant to that of graphene, the distance is more accurate at 2.82 Å while the n-doping is rather small. Both cases are seen in Figure 3.5. These cases demonstrates

the sensitivity of calculations on different parameters.

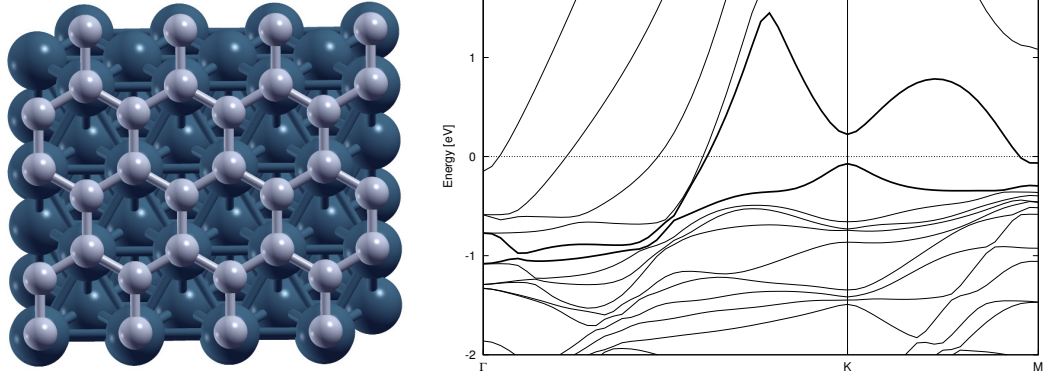


Figure 3.4: The on-top geometry of graphene on Ni(111) and the band structure of the graphene/Ni(111) system.

### 3.4 CNTs on Graphene on Metals

In calculating the CNT(8,0)/graphene/Cu(111) interface, the lattice parameters are fixed to that of graphene and van-der Waals corrections are included. First, the graphene+Cu(111) system was calculated without the carbon nanotube. As the unit cell grows, the number of metallic layers is reduced to 3 from 5 in order to save computational time and the last layer was kept fixed. In this case, the graphene-Cu(111) distance was calculated to be 3.35 Å.

The CNT(8,0)/graphene/Cu(111) system both the CNT weakly interacting with graphene and CNT that formed a single C–C bond was considered. The systems has 112 atoms in total. Upon optimization for the physisorption case, the graphene-CNT distance was found to be 3.24 Å which is the same as the CNT-graphene separation for isolated graphene. The nanotube causes a slight curvature on the graphene layer. The graphene-Cu distance is 3.2 Å beneath the nanotube and it is 3.4 Å far from the nanotube.

For the case in which the CNT is bonded to graphene, The C–C bond length increased slightly to 1.63 Å from 1.62 Å in isolated graphene. The graphene-Cu(111) distance decreased slightly ranging from 3.15 Å to 3.25 Å apart from the cusp underneath the

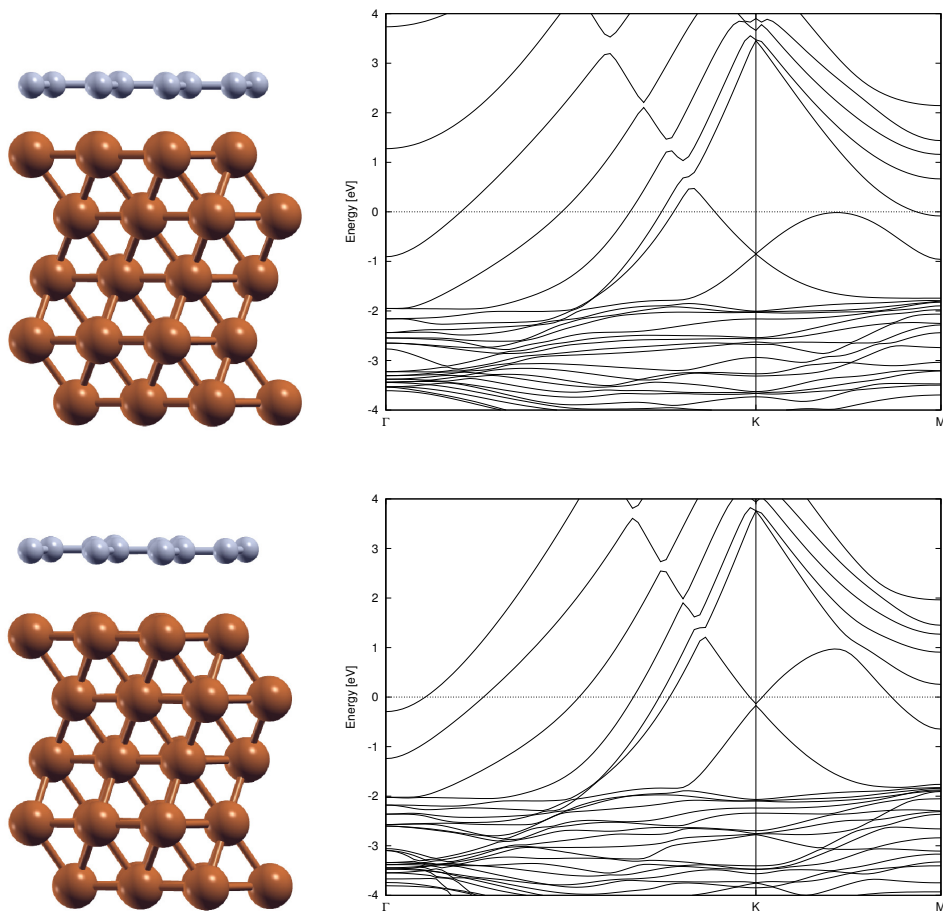


Figure 3.5: The relaxed configurations and band structures of graphene on Cu(111) calculated with the lattice parameter of graphene (top) and lattice parameter of the metal (bottom).

CNT which is at  $3.74 \text{ \AA}$ .

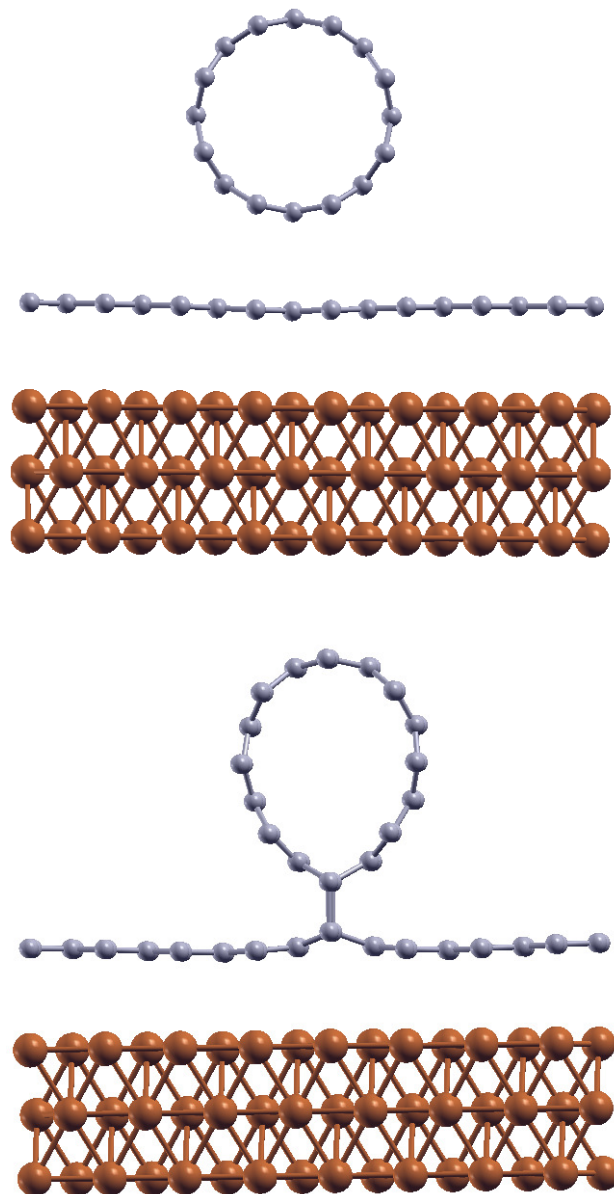


Figure 3.6: The CNT(8,0) interacting through van-der Waals forces (top) and a single C–C bond (bottom) with graphene on Cu(111).



## CHAPTER 4

### INTERACTION OF IDEAL AND DEFECTED GRAPHENE WITH CYCLOHEXANES

In this chapter, the interaction of cyclohexane (c-hexane,  $C_6H_{12}$ ) and its dehydrogenated derivatives, cyclohexyl radical (c-hexyl,  $C_6H_{11}^*$ ) and cyclohexene molecule (c-hexene,  $C_6H_{10}$ ) on both pristine and defected graphene is explored. In our defect calculations, we include a single vacancy and a C adatom as well as a substitutionally doped N atom. While  $C_6H_{12}$  only has completely saturated  $sp^3$  bonds,  $C_6H_{10}$  has a mixture of  $sp^2$  and  $sp^3$  bonds.  $C_6H_{11}^*$ , on the other hand, is a radical with high reactivity. The choice of these three molecules provides a platform for diverse modes of bonding and band structure manipulation.

#### 4.1 Computational Details

Vanderbilt ultrasoft pseudopotentials [71] with PBE-GGA and PZ-LDA exchange-correlation functionals were used [55]. For systems in which dispersive forces are predicted to play an important role, a van der Waals correction to the exchange-correlation functional was present and executed fully self-consistently as implemented in Quantum Espresso through the Soler algorithm [59]. VDW-DF2 type Van-der Waals functionals were used with the C09 exchange (VDW2-C09) [44, 15]. A kinetic energy cut-off of 30 Ryd and an augmentation cut-off of 300 Ryd were used in all calculations which gave well-converged values for both graphene and molecules. Marzari-Vanderbilt type cold smearing with a broadening of 0.02 eV was employed for Brillouin zone integration [49]. A vacuum separation of at least 12 Å was present

in all calculations to prevent interaction between periodic images.

On pristine graphene, molecules with  $\Theta=1/36$  ML and  $\Theta=1/9$  ML coverages were considered which correspond to a surface density of one molecule per  $6\times 6$  and  $3\times 3$  graphene unit cells respectively. The  $1/36$  ML coverage offers an intermolecular distance of at least  $10 \text{ \AA}$  while  $1/9$  ML corresponds to a full coverage as the molecules start to intertwine at denser concentrations. For defected graphene, the interaction of a molecule with a single defect per  $6\times 6$  unit cell is considered. Monkhorst-Pack meshes of  $6\times 6\times 1$  and  $3\times 3\times 1$  k-points were used for the  $3\times 3$  and  $6\times 6$  cells respectively. The optimal structures were obtained through a full relaxation of the systems using the BFGS optimization algorithm [12, 22, 26, 63] with a force convergence threshold of  $0.025 \text{ eV/\AA}$ .

The adsorption energies are calculated from:

$$E_{ads} = E_{molecule+gr} - E_{gr} - E_{molecule} \quad (4.1)$$

where  $E_{molecule+gr}$  is the total energy of the combined system,  $E_{gr}$  is the energy of the pristine or defected graphene sheet and  $E_{molecule}$  is the energy of an isolated  $C_6H_{12}$ ,  $C_6H_{11}$  or  $C_6H_{10}$  molecule, all calculated with the same computational parameters.

## 4.2 $C_6H_{12}$ , $C_6H_{11}^*$ and $C_6H_{10}$

The geometric optimization for isolated molecules was carried out in a large cubic unit cell at the  $\Gamma$  point using the PBE-GGA pseudopotential. Cyclohexane  $C_6H_{12}$  is mostly found in the chair conformation as seen in Figure 4.1. The cyclohexane ring deviates from a planar hexagon in order to reduce the torsional strain and the C-C-C angles decrease to about  $109.5$  degrees. It is the most unreactive and stable cycloalkane. The calculated C-C-C bond angle and C-C bond length for the  $C_6H_{12}$  molecule are  $111.4^\circ$  and  $1.5328 \text{ \AA}$  respectively. The axial H atoms which are perpendicular to the molecular mean plane and the equatorial H atoms which surround the  $C_6H_{12}$  ring have slightly different H-C distances with  $d_{equatorial}=1.1043 \text{ \AA}$  and  $d_{axial}=1.1006 \text{ \AA}$ . The deviation of equatorial H atoms from the mean plane is  $16.3^\circ$ . The Highest Occupied Molecular Orbital (HOMO) and Lowest Occupied Molecular Orbital (LUMO) gap of the molecule is computed to be  $6.42 \text{ eV}$ .



$C_6H_{11}^*$  has a slightly distorted chair geometry with an increased C–C–C bond angle of  $119.1^\circ$  and a decreased C–C bond length of  $1.4775 \text{ \AA}$  around the C atom which lacks one hydrogen while the remaining bond angles remain about  $111^\circ$ . The single H atom is positioned equatorially, leaving two axial H atoms on one side of the molecule. The H–C bond length of this atom is the shortest among others with a value of  $1.0892 \text{ \AA}$  while the closest two axial H atoms have H–C distances of  $1.1160 \text{ \AA}$ . Having an odd number of valence electrons,  $C_6H_{11}^*$  has a half-filled orbital.

The  $C_6H_{10}$  molecule has two adjacent C atoms bonded to a single H atom. Its stable conformer is the half-chair geometry in which the these two C atoms and the two C atoms bonded to them are in the same plane while two C atoms are in the opposite sides of this plane. The C–C–C angles between the four coplanar contiguous C atoms are  $123.5^\circ$  and they are  $111.1^\circ$  in the remaining part. The C–C bond length between the C atoms with a single H is calculated to be  $1.34 \text{ \AA}$ , between these C atoms and their neighbors it is  $1.50 \text{ \AA}$  and the bond length is  $1.53 \text{ \AA}$  for the remaining three C–C bonds. The C–H distance is  $1.09 \text{ \AA}$  for the single H atoms which are equatorially positions, and it is about  $1.10 \text{ \AA}$  with small differences at the third decimal for the remaining C–H bonds. The HOMO-LUMO gap of this molecule is computed to be  $5.07 \text{ eV}$ . The relaxed structures and HOMO-LUMO plots of the molecules are presented in Figure 4.1. All of these results compare well with experimental data.

### 4.3 Molecules on Ideal Graphene

A  $C_6H_{12}$  molecule on a  $6 \times 6$  graphene can be treated as an isolated molecule as the smallest intermolecular distance between periodic images is about  $10.4 \text{ \AA}$ . There are 90 atoms in the  $6 \times 6$  graphene+ $C_6H_{12}$  system. Due to the stability and unreactivity of both structures,  $C_6H_{12}$  weakly interacts with graphene and upon relaxation the system easily traps into a local minima. Thus in order to determine the most preferred sites of  $C_6H_{12}$  on graphene, the systems were relaxed starting from 14 distinct initial configurations formed by rotating and shifting the molecule which are seen in Figure 4.3. The configurations in which the mean-plane of the molecule is parallel and perpendicular to graphene were both considered. The adsorption energies and graphene-molecule distances obtained from these configurations are listed in Table

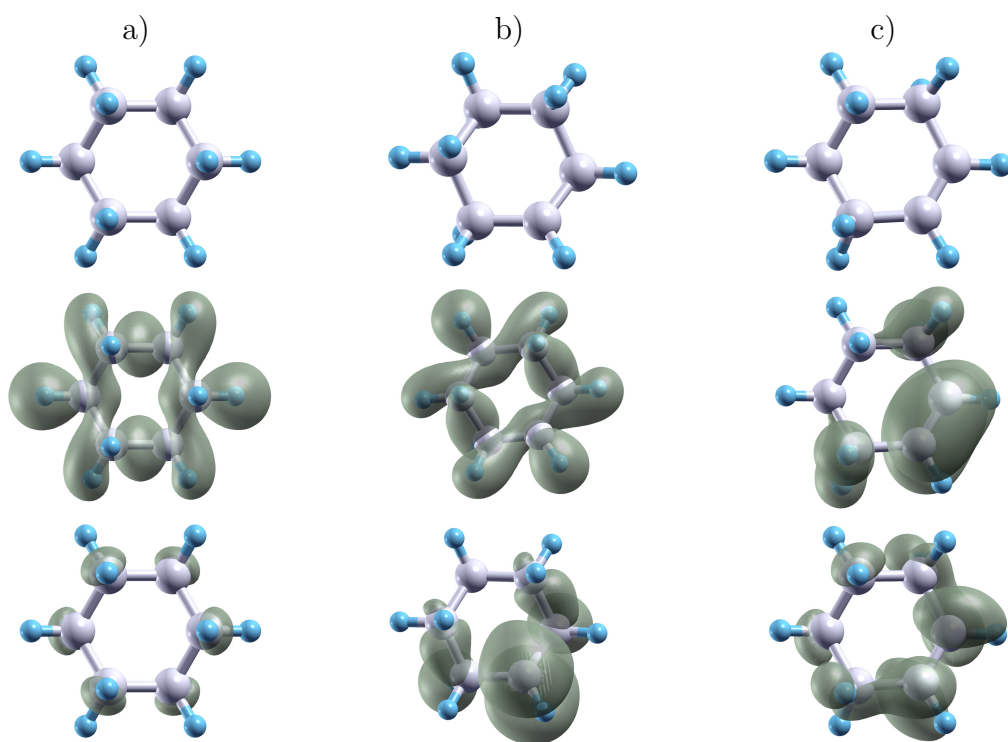


Figure 4.1: Relaxed structures of the (a) C<sub>6</sub>H<sub>12</sub>, (b) C<sub>6</sub>H<sub>11</sub><sup>\*</sup> and (c) C<sub>6</sub>H<sub>10</sub> molecules along with the HOMO (middle panel) and LUMO (lower panel) orbitals

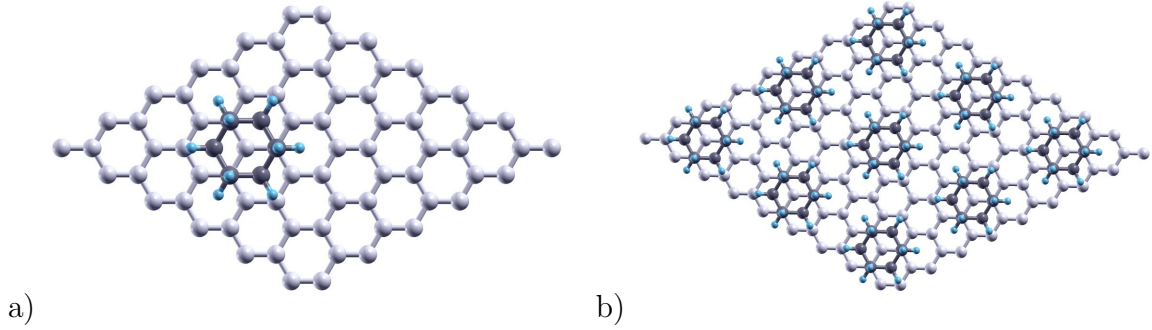


Figure 4.2: The  $C_6H_{12}$  molecule on pristine graphene with (a)  $1/9$  ML and (b)  $1/36$  ML concentrations.

4.1. The molecule induces small curvatures in the graphene layer. Thus the distances were taken as the vertical separation of the average value in the z-direction of C atoms in graphene and the H atom of the molecule that is closest to the graphene layer.

We found that the preferred geometry of a  $C_6H_{12}$  molecule on graphene is a parallel configuration in which the axial H atoms of the molecule facing the graphene layer are located on top of the centers of the empty hexagonal sites of the honeycomb lattice of graphene as seen in Figure 4.4. In the optimized structure, the  $C_6H_{12}$  molecule is located at a distance of  $2.48 \text{ \AA}$  and the adsorption energy is  $321 \text{ meV}$ . Without the vdW correction the PBE-GGA calculation yields the molecule-graphene distance as  $3.1 \text{ \AA}$  and a binding energy of only  $43 \text{ meV}$ . Several metastable structures were obtained from other initial configurations which yielded slightly lower adsorption energies by  $10$  to  $30 \text{ meV}$  for parallel geometries and by about  $0.1 \text{ eV}$  for perpendicular geometries.

Upon increasing the  $C_6H_{12}$  concentration from  $\Theta=1/36$  ML to  $\Theta=1/9$  ML as seen in Figure 4.2, the graphene-molecule distance increased from  $2.48 \text{ \AA}$  to  $2.49 \text{ \AA}$ . The adsorption energy of the  $C_6H_{12}$  monolayer is  $3 \text{ meV}$  higher than the single molecule, it is  $324 \text{ meV}$ . The total energy of the  $3 \times 3$  molecules is  $64 \text{ meV}$  lower than the  $6 \times 6$  concentration. This slight difference may be interpreted as a tendency to cluster on pristine graphene.

The band structure for the non-covalent interaction of the  $C_6H_{12}$  molecule with pristine graphene reveals no deviation around the K-point from ideal graphene's band

Table 4.1: Distances and binding energies of  $C_6H_{12}$  and  $C_6H_{11}^*$  on ideal graphene layer at different sites.

	Site	Parallel		Site	Perpendicular	
		d[Å]	$E_b$ [meV]		d[Å]	$E_b$ [meV]
$C_6H_{12}$	A	2.59	290	A	2.59	191
	B	2.58	289	B	2.43	212
	BC	2.47	312	C	2.56	188
	C	2.48	323	D	2.56	207
	Ar	2.58	300	Ar	2.56	200
	Br	2.57	302	Br	2.58	192
	BCr	2.49	300	Cr	2.38	189
$C_6H_{11}^*$	A	1.69 (C-C)	352	A	2.36	352
	B	1.66 (C-C)	543	B	1.65(C-C)	692
	BC	2.45	467	C	1.65(C-C)	698
	C	2.48	458	D	2.37	308
	Ar	2.44	462	Ar	2.42	351
	Br	2.50	443	Br	1.64(C-C)	687
	BCr	1.67 (C-C)	538	Cr	2.27	305

structure as seen in Figure 4.4. Additional states from the molecule fell on the conduction and valence parts. The population analysis using the Löwdin methods reveals that only 0.02 e is lost by the  $C_6H_{12}$  molecule upon adsorption.

Similarly, a systematic investigation of the preferred geometries for  $C_6H_{11}^*$  was conducted by examining the same initial configurations considered for the  $C_6H_{12}$  molecule.  $C_6H_{11}^*$  forms a carbon-carbon bond in the equatorial conformation with pristine graphene as seen in Figure 4.4. The bond length is 1.65 Å and the binding energy is 0.70 eV calculated by including van-der Waals corrections. Dispersive forces makes an important contribution to this rather weak C-C bond as the binding energy is just 0.12 eV when calculated with PBE only. Upon adsorption the flat structure of graphene is deformed and the three carbon bonds surrounding the binding carbon atom of graphene are extended to 1.50 Å. The less stable axial conformation has a binding energy of 0.54 eV and the C-C bond length is 1.66 Å. The charge transfer is from molecule to graphene and the lost charge is 0.01 e by Lowdin analysis. The fact that this value is even smaller than the charge transfer in  $C_6H_{12}$ /graphene interaction

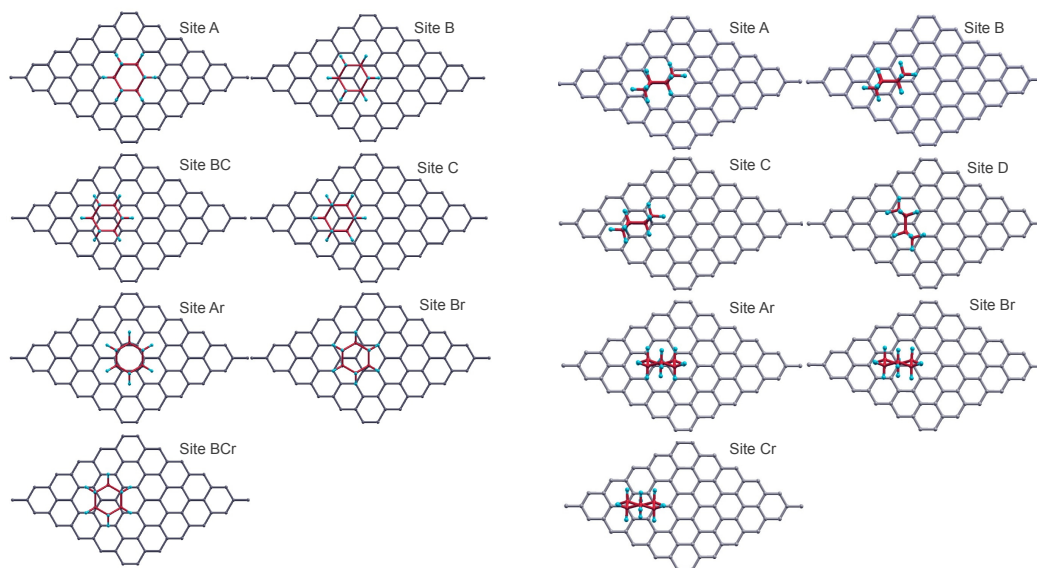


Figure 4.3: Different initial configurations for  $C_6H_{12}$  on pristine graphene.

even though the molecule is bonded by a C–C bond may be attributed to the inaccuracy of the Lowdin method. As seen in the band structure of the  $C_6H_{11}^*$ +graphene system in Figure 4.4, one flat band coincides with the Fermi level rendering the system metallic. Furthermore, the degeneracy of the pi bands is lifted.

Similar to  $C_6H_{12}$ , the  $C_6H_{10}$  molecule physisorbes on pristine graphene. At the on-top site as seen in Figure 4.4, the calculated adsorption energy is 391 meV and the graphene-molecule distance is 2.45 Å.  $C_6H_{10}$  has a slightly larger adsorption energy and stabilizes at a smaller distance than  $C_6H_{12}$ . Again this interaction doesn't result in a significant change around the Dirac point as seen in the band structure in Figure 4.4 apart from a molecular band at 1.5 eV below the Fermi level.

#### 4.4 Defect-Bonded Molecules

Our calculations showed that the interaction of the  $C_6H_{12}$  molecule with defected graphene has a non-covalent nature both for a single vacancy and a carbon adatom as with the pristine graphene. In the case of a single vacancy, the adsorption energy is calculated without including spin degrees of freedom as spin-polarized calculations

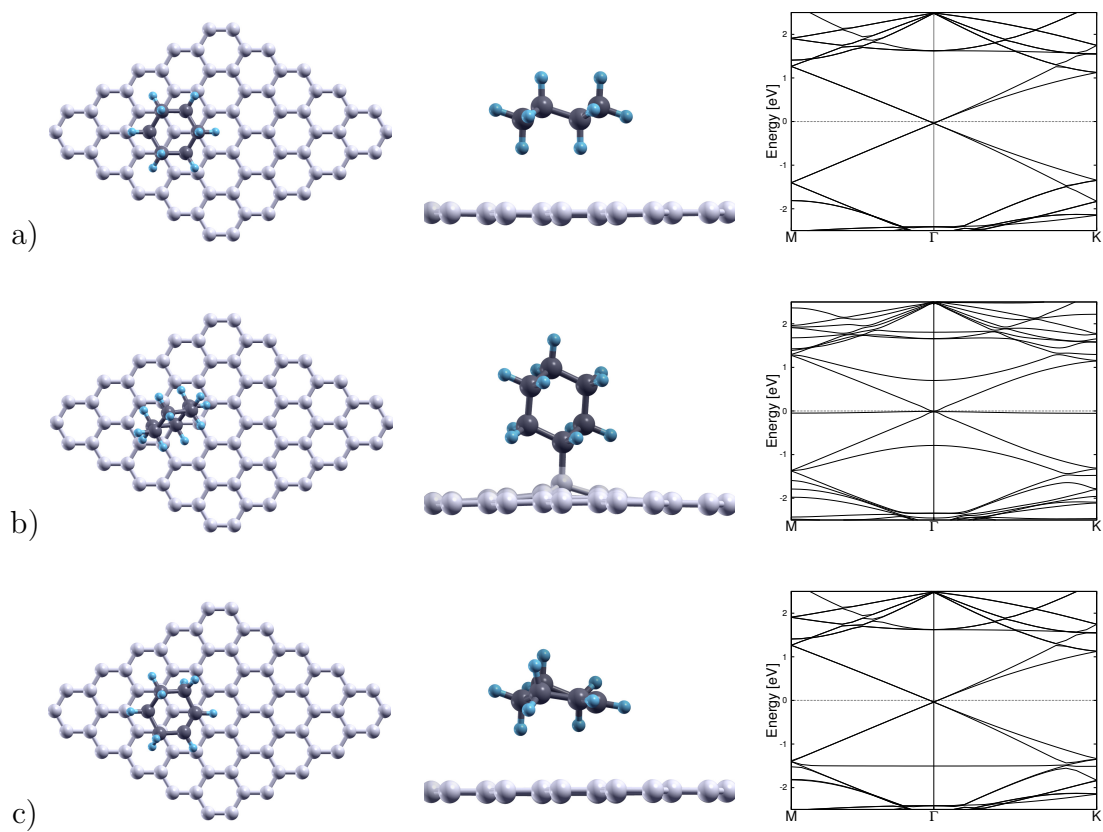


Figure 4.4: Geometry and band structure of  $C_6H_{12}$  (a),  $C_6H_{11}^*$  (b) and  $C_6H_{10}$  (c) on pristine graphene

cannot be conducted in conjunction with the van-der Waals functionals. A spin polarized GGA calculation yields no binding at all, and an LSDA computation may be unreliable due to the underestimation of the lattice constant of graphene which may be more important in the presence of a vacancy. Upon adsorption as seen in Figure 4.5, the molecule causes the planarity around the vacancy to disturb by attracting the unsaturated C atom. The vertical distance of this atom from the mean plane of graphene is 0.45 Å. The adsorption energy in this case is 0.29 eV which is slightly smaller than pristine graphene and the distance of the molecule to the mean graphene plane is 2.67 Å. As a side note, a less preferred configuration in which the molecule is rotated such that an axial H atom is positioned on top of the unsaturated C atom has also been considered and this time the flatness is disturbed in the opposite way, i.e., the molecule repelled the C atom.

The interaction of  $C_6H_{12}$  with graphene with a single C adatom is rather weak with a binding energy of only 0.12 eV and induces no visible changes in the band structure as seen in Figure 4.6. For this system we also considered an initial condition in which the molecule-graphene distance is considerably small, which can be physically thought as forcing the molecule towards the defect. Then, upon geometric optimization both structures become completely disrupted, one hydrogen atom spontaneously moved to the adatom and we ended up with  $C_6H_{11}^*$  with a CH group bonded to ideal graphene surface.

The  $C_6H_{11}^*$  molecule makes a C-C bond with the unsaturated C atom at the single vacancy which is presented in Figure 4.5. Upon adsorption the total magnetic moment of the system becomes zero, i.e., spin polarization disappears. The adsorption energy is 3.26 eV. The length of the C-C bond is 1.54 Å. The flatness is again disrupted as the unsaturated C atom bend upwards toward the molecule and the bond lengths of this atom increase from 1.36 Å to 1.42 Å. According to Lowdin population analysis, the charge transfer from the molecule to graphene is calculated to be 0.03 e which is again rather small. In the  $C_6H_{11}^*/$ single vacancy system, the band structure around the Fermi level at the gamma point did not change. However, the flat band about 0.5 eV below the Fermi level disappeared.

Adsorption of the  $C_6H_{11}^*$  molecule to the C adatom is again through a C-C bond as

seen in Figure 4.6. The molecule adsorbs at equatorial conformation with a binding energy of 3.59 eV. The binding energy of adsorption at the axial conformation is 78 meV lower than this value. The C-C bond length is 1.46 Å. In this case, the Fermi level is shifted upwards so that the flat band coincides with the Fermi level and the shapes of the bands around Fermi level also changes slightly resembling the band structure of bilayer graphene.

Cyclohexene is physisorbed on graphene with a single vacancy as cyclohexane in a rotated configuration in which the unsaturated C atom is repelled from the molecule as seen in Figure 4.5. The binding energy was calculated to be 0.36 eV and the distance is 2.49 Å. The molecule-graphene distance is lower and the binding energy is higher than cyclohexane. Again, spin degrees of freedom were not taken into account and the band structure reveals no differences than the clean surface.

On the adatom, this time cyclohexene binds through two carbon-carbon bonds as seen in Figure 4.6. The bond lengths of these bonds are Å and the binding energy is calculated as eV. In the band structure for this interaction, the flat band near the Fermi level is removed and a tiny gap is observed. Even though this band gap may be due to computational errors, there is a chance that the system is rendered a small gap semiconductor upon adsorption of C<sub>6</sub>H<sub>10</sub>.

#### 4.5 Molecules on N-Doped Graphene

Similar to pristine graphene, both C<sub>6</sub>H<sub>12</sub> and C<sub>6</sub>H<sub>10</sub> physisorbes on N-doped graphene. In the on-top geometry as seen in Figure 4.7, the binding energy is the same for C<sub>6</sub>H<sub>12</sub> (0.32 eV) while it is slightly increased to 0.41 eV from 0.39 eV for C<sub>6</sub>H<sub>10</sub>. There is also a slight increase in the molecule-graphene distance by 0.01 Å for C<sub>6</sub>H<sub>12</sub> while the separation remained the same for C<sub>6</sub>H<sub>10</sub>. Again, these weak interactions does not induce visible changes in the band structure and the system remains negatively doped as seen in Figure 4.7.

The C<sub>6</sub>H<sub>11</sub>\* binds to the substituted N-atom through a C-N bond with a bond length of 1.62 Å as presented in Figure 4.7. Even though this bond length is shorter than the length of the C-C bond which forms during the molecule's adsorption on pristine



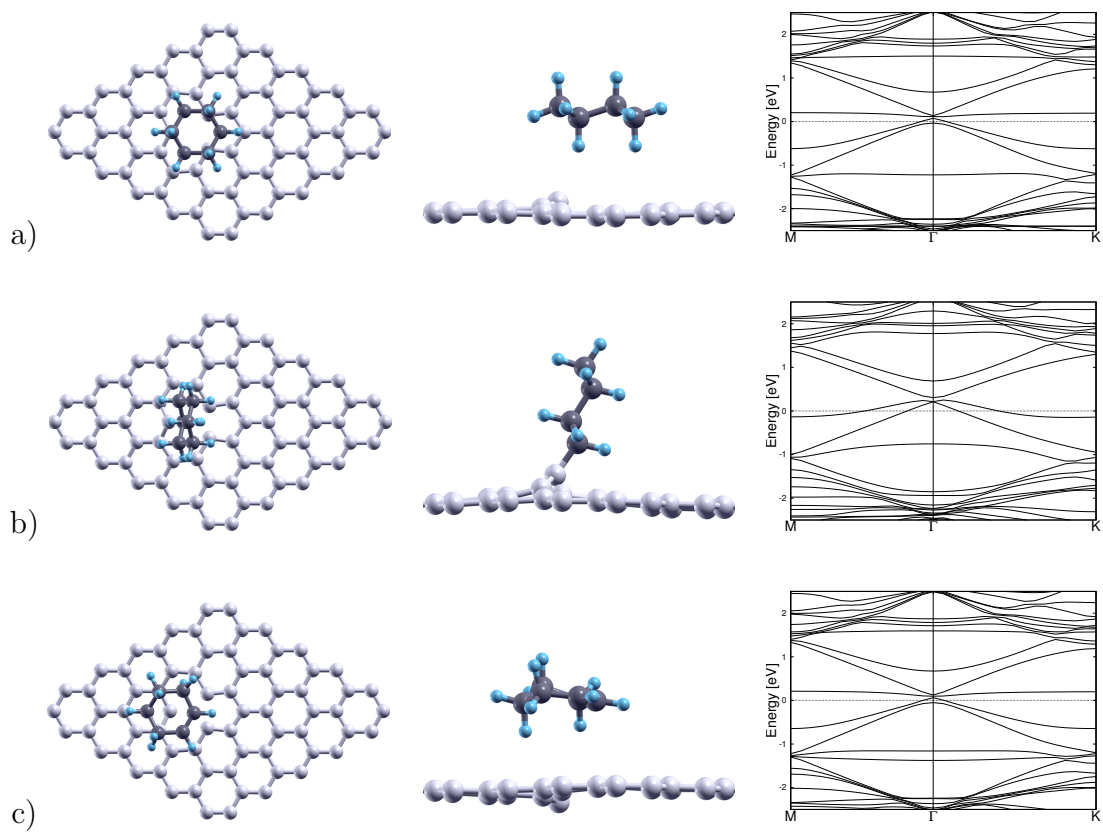


Figure 4.5: Geometry and band structure of,  $C_6H_{12}$  (a),  $C_6H_{11}^*$  (b) and  $C_6H_{10}$  (c) interacting with a single vacancy.

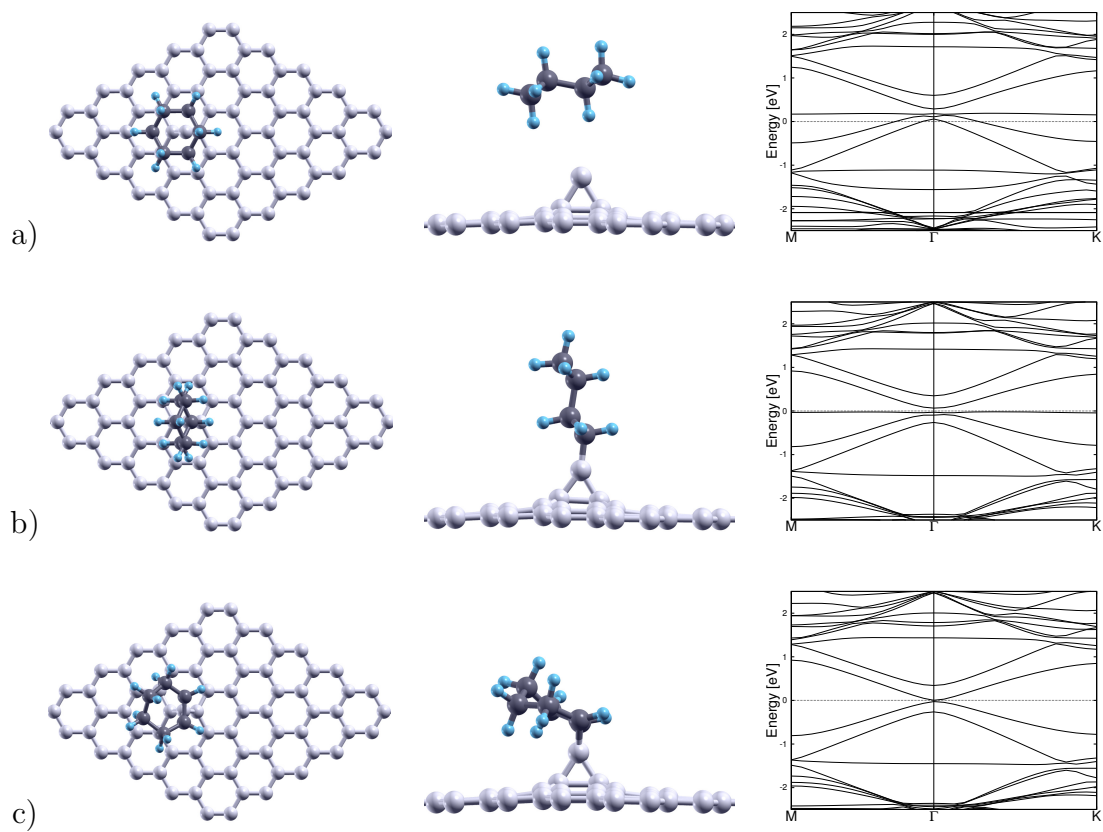


Figure 4.6: Geometry and band structure of,  $C_6H_{12}$  (a),  $C_6H_{11}^*$  (b) and  $C_6H_{10}$  (c) interacting with a single C adatom.

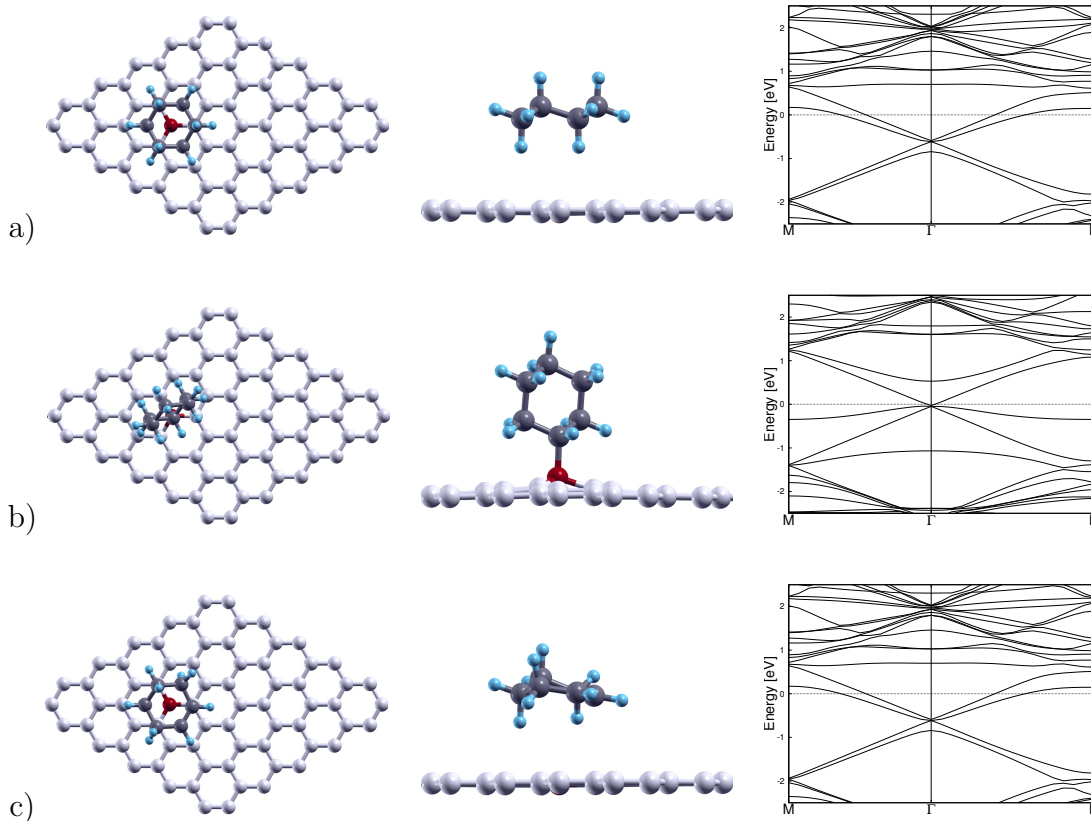


Figure 4.7: Geometry and band structure (a)  $C_6H_{12}$ , (b)  $C_6H_{11}^*$  and (c)  $C_6H_{10}$  interacting with N-doped graphene.

graphene, the binding energy is lower at 0.42 eV. This low value for the binding energy is due to the structural strain in the graphene layer caused by the interaction. Upon adsorption, the molecule attracts the N atom and the lengths of the C-N bonds in the graphene layer increase by 7% from 1.41 Å to 1.51 Å. This interaction causes the Fermi level to shift upwards and reverses the N-doping.

All the calculated binding energies  $E_b$  and distances  $d$  of the  $C_6H_{12}$ ,  $C_6H_{11}^*$  and  $C_6H_{10}$  molecules adsorbed on pristine graphene, graphene with a single vacancy, graphene with a C adatom and N-Doped graphene are summarized in Table 4.2.

Table 4.2: Summary of the binding energies  $E_b$ , distances  $d$  of the molecules adsorbed on pristine graphene, graphene with a single vacancy, graphene with a C adatom and N-Doped graphene

	Pristine		Single Vacancy		C Adatom		N-Doped	
	$E_b$ [eV]	$d$ [Å]	$E_b$ [eV]	$d$ [Å]	$E_b$ [eV]	$d$ [Å]	$E_b$ [eV]	$d$ [Å]
$C_6H_{12}$	0.32	2.48	0.29	2.67	0.12	3.12	0.32	2.49
$C_6H_{11}^*$	0.70	1.65	3.26	1.54	3.59	1.46	0.42	1.62
$C_6H_{10}$	0.39	2.45	0.36	2.49	3.44	1.48	0.41	2.45

## CHAPTER 5

### CONCLUSION

In this thesis, properties of ideal and defected graphene structures, CNT/graphene interactions, effects of metal support on graphene, the CNT+graphene+metal interface and interaction of cyclohexane and its dehydrogenated derivatives with pristine and defected graphene structures are studied using density functional theory. We have used van-der Waals functionals at the vdW-DF2 level fully self-consistently for interactions involving van-der Waals forces. Corresponding pseudopotentials were generated to use in combination with vdW functionals. Different functionals were benchmarked with graphite and bilayer graphene and we found that vdW-DF2-c09x functionals yield the most accurate results for graphene-based structures in accordance with previous studies [29].

The interaction of horizontally aligned (6,0) and (8,0) nanotubes on an isolated graphene layer is investigated. Two different adsorption modes for the CNT on graphene was found: it is either physisorbed or interacts with graphene via single or double C-C bonds accompanied with a deformation of both structures. Similar results were previously theoretically found for the CNT-CNT junctions [17]. The CNT(6,0) is metallic, whereas The CNT(8,0) is a small gap semiconductor and the CNT(8,0)+graphene system remains semiconducting when the interaction is through van-der Waals forces, while it becomes metallic as C-C bonds form. Even though direct experimental evidence is lacking which indicates the formation of such bonds and the electronic structure of similar systems, our results support various experimental findings regarding the mixed semiconductor/metal nature of CNT/graphene hybrid films(ref).

In order to explore both the potential of the graphene to be used in the cyclohexane-

oxidation processes and the potential of cyclohexane-type molecules to functionalize graphene, we investigated the interaction of cyclohexane, cyclohexyl and cyclohexene with pristine graphene and graphene defected with a single vacancy, a single C adatom and graphene doped with a single N atom. We found that the cyclohexane molecule weakly interacts with all the pristine and defected graphene structures without introducing any significant changes in the band structure. After rigorous analysis of different adsorption sites on pristine graphene we found that the molecule prefers the configurations in which it can maximize the number of hydrogen atoms located at the centers of the hexagons of the honeycomb lattice of graphene. We found that the binding energies for this molecule are about 0.3 eV for all the considered surfaces, except for the adatom with a binding energy of only 0.12 eV.

Cyclohexyl, which is a radical that is one H atom short of c-hexane binds to each structure with a single C–C bond. It introduces a new state at the Fermi level for pristine graphene. Upon the molecule's absorption to the unsaturated C atom at the single vacancy, it neutralizes the spin-polarization of the system while at the same time increasing n-doping by causing a downward shift of the bands. Another notable result is that the adsorption of c-hexyl to the N atom on N-doped graphene is that it reverses the n-doping of the system.

Except for the adatom, the c-hexene molecule physisorbs to each graphene structure with adsorption energies slightly larger than those of c-hexane. This molecule strongly binds to the adatom through two C–C bonds. Upon adsorption, the molecule possibly causes the opening of a very small band gap. Another notable point is that c-hexene binds to N-doped graphene with a slightly larger energy than pristine graphene which supports the findings in [81], whereas the binding energies are the same for c-hexane for both structures.

## REFERENCES

- [1] R. Balog, M. Andersen, B. Jørgensen, Z. Sljivancanin, B. r. Hammer, A. Baraldi, R. Larciprete, P. Hofmann, L. Hornekær, and S. Lizzit. Controlling hydrogenation of graphene on Ir(111). *ACS nano*, 7(5):3823–32, 2013.
- [2] F. Banhart, J. Kotakoski, and A. V. Krasheninnikov. Structural defects in graphene. *ACS nano*, 5(1):26–41, Jan. 2011.
- [3] V. Barone, M. Casarin, D. Forrer, M. Pavone, M. Sambri, A. Vittadini, C.-i. Village, V. Marzolo, F. Ii, C. Paolo, C. Universitario, M. Sant, and V. Cintia. Role and effective treatment of dispersive forces in materials : Polyethylene and graphite crystals as test cases. 2008.
- [4] M. Batzill. The surface science of graphene: Metal interfaces, CVD synthesis, nanoribbons, chemical modifications, and defects. *Surface Science Reports*, 67(3-4):83–115, Mar. 2012.
- [5] M. a. Bissett, M. Tsuji, and H. Ago. Strain engineering the properties of graphene and other two-dimensional crystals. *Physical chemistry chemical physics : PCCP*, 16(23):11124–38, 2014.
- [6] E. W. Bittner, M. R. Smith, and B. C. Bockrath. Characterization of the surfaces of single-walled carbon nanotubes using alcohols and hydrocarbons : a pulse adsorption technique. *Carbon*, 41:1231–1239, 2003.
- [7] D. W. Boukhvalov. DFT modeling of the covalent functionalization of graphene: from ideal to realistic models. *RSC Advances*, 3(20):7150, 2013.
- [8] D. W. Boukhvalov and M. I. Katsnelson. Chemical functionalization of graphene with defects. *Nano Letters*, 8(12):4373–4379, 2008.
- [9] D. W. Boukhvalov and M. I. Katsnelson. Chemical functionalization of graphene. *Journal of Physics: Condensed Matter*, 21(34):344205, 2009.
- [10] L. Brey and H. Fertig. Electronic states of graphene nanoribbons studied with the Dirac equation. *Physical Review B*, (23):235411, 2006.
- [11] C. G. Broyden. A class of methods for solving nonlinear simultaneous equations. *Mathematics of computation*, pages 577–593, 1965.
- [12] C. G. BROYDEN. The convergence of a class of double-rank minimization algorithms: 2. the new algorithm. *IMA Journal of Applied Mathematics*, 6(3):222–231, 1970.

- [13] a. H. Castro Neto, N. M. R. Peres, K. S. Novoselov, and a. K. Geim. The electronic properties of graphene. *Reviews of Modern Physics*, 81(1):109–162, Jan. 2009.
- [14] C. Coletti, C. Riedl, D. S. Lee, B. Krauss, L. Patthey, K. von Klitzing, J. H. Smet, and U. Starke. Charge neutrality and band-gap tuning of epitaxial graphene on SiC by molecular doping. *Physical Review B*, 81(23):235401, 2010.
- [15] V. R. Cooper. Van der waals density functional: An appropriate exchange functional. *Physical Review B*, 81(16):1–4, Apr. 2010.
- [16] O. Cretu, A. V. Krasheninnikov, J. A. Rodríguez-Manzo, L. Sun, R. M. Nieminen, and F. Banhart. Migration and localization of metal atoms on strained graphene. *Phys. Rev. Lett.*, 105:196102, Nov 2010.
- [17] S. Dag, R. Senger, and S. Ciraci. Theoretical study of crossed and parallel carbon nanotube junctions and three-dimensional grid structures. *Physical Review B*, 70(20):1–9, Nov. 2004.
- [18] E. R. Davidson. The iterative calculation of a few of the lowest eigenvalues and corresponding eigenvectors of large real-symmetric matrices. *Journal of Computational Physics*, 17(1):87 – 94, 1975.
- [19] E. Díaz, S. Ordóñez, and A. Vega. Adsorption of volatile organic compounds onto carbon nanotubes , carbon nanofibers , and high-surface-area graphites. *J Colloid Interf Sci*, 305:7–16, 2007.
- [20] M. Dion, H. Rydberg, and E. Schröder. Van der waals density functional for general geometries. *Physical Review Letters*, 1(June):22–25, 2004.
- [21] J. M. Englert, C. Dotzer, G. Yang, M. Schmid, C. Papp, J. M. Gottfried, H.-P. Steinrück, E. Spiecker, F. Hauke, and A. Hirsch. Covalent bulk functionalization of graphene. *Nature Chemistry*, 3:279–286, 2010.
- [22] R. Fletcher. A new approach to variable metric algorithms. *The Computer Journal*, 13(3):317–322, 1970.
- [23] V. Georgakilas, M. Otyepka, A. B. Bourlinos, V. Chandra, N. Kim, K. C. Kemp, P. Hobza, R. Zboril, and K. S. Kim. Functionalization of graphene: Covalent and non-covalent approaches, derivatives and applications. *Chemical Reviews*, 112(11):6156–6214, 2012.
- [24] P. e. a. Giannozzi. QUANTUM ESPRESSO: a modular and open-source software project for quantum simulations of materials. *Journal of physics. Condensed matter : an Institute of Physics journal*, 21(39):395502, Sept. 2009.
- [25] G. Giovannetti, P. Khomyakov, G. Brocks, V. Karpan, J. van den Brink, and P. Kelly. Doping Graphene with Metal Contacts. *Physical Review Letters*, 101(2):4–7, July 2008.



- [26] D. Goldfarb. A Family of Variable-Metric Methods Derived by Variational Means. *Mathematics of Computation*, 24(109):23–26, Jan. 1970.
- [27] S. Grimme. Accurate description of van der waals complexes by density functional theory including empirical corrections. *Journal of Computational Chemistry*, 25(12):1463–1473, 2004.
- [28] S. Grimme, T. O. Chemie, and O.-c. I. D. U. Münster. Semiempirical gga-type density functional constructed with a long-range dispersion correction. 16, 2006.
- [29] I. Hamada and M. Otani. Comparative van der Waals density-functional study of graphene on metal surfaces. *Physical Review B*, 82(15):1–4, Oct. 2010.
- [30] D. R. Hamann, M. Schlüter, and C. Chiang. Norm-conserving pseudopotentials. *Phys. Rev. Lett.*, 43:1494–1497, Nov 1979.
- [31] R. W. Havener, Y. Liang, L. Brown, L. Yang, and J. Park. Van Hove Singularities and Excitonic Effects in the Optical Conductivity of Twisted Bilayer Graphene. *Nano Letters*, 14:3353–3357, 2014.
- [32] P. Hohenberg and W. Kohn. Inhomogeneous electron gas. *Physical Review*, 155(1962), 1964.
- [33] Y. Huang, J. Liang, and Y. Chen. The application of graphene based materials for actuators. *Journal of Materials Chemistry*, 22(9):3671, 2012.
- [34] S. Iijima. *Nature*, 56(354), 1991.
- [35] S. Jang, H. Jang, Y. Lee, D. Suh, S. Baik, B. H. Hong, and J.-H. Ahn. Flexible, transparent single-walled carbon nanotube transistors with graphene electrodes. *Nanotechnology*, 21(42):425201, 2010.
- [36] S. H. Jin, D. H. Kim, G. H. Jun, S. H. Hong, and S. Jeon. *ACS nano*, 7(2):1239–45, 2013.
- [37] F. Karlický and M. Otyepka. Band Gaps and Optical Spectra of Chlorographene, Fluorographene and Graphane from  $G_0W_0$ ,  $GW_0$  and  $GW$  Calculations on Top of PBE and HSE06 Orbitals. *Journal of Chemical Theory and Computation*, 9(9):4155–4164, 2013.
- [38] N. K. S. G. A. K. Katsnelson, M. I. Chiral tunneling and the Klein paradox in graphene. *Nature Phys.*, 2:620–625, 2006.
- [39] W. Kohn and L. Sham. Self-consistent equations including exchange and correlation effects. 385(1951), 1965.
- [40] A. Kokalj. Xcrysden a new program for displaying crystalline structures and electron densities. *Journal of Molecular Graphics and Modelling*, 17(3–4):176–179, 1999.

- [41] T. Kuila, S. Bose, A. Kumar, and P. Khanra. Progress in Materials Science Chemical functionalization of graphene and its applications. *Progress in Materials Science*, 57(7):1061–1105, 2012.
- [42] D. C. Langreth, B. I. Lundqvist, S. D. Chakarova-Käck, V. R. Cooper, M. Dion, P. Hyldgaard, a. Kelkkanen, J. Kleis, L. Kong, S. Li, P. G. Moses, E. Murray, a. Puzder, H. Rydberg, E. Schröder, and T. Thonhauser. A density functional for sparse matter. *Journal of physics. Condensed matter : an Institute of Physics journal*, 21(8):084203, Feb. 2009.
- [43] K. Lee, K. Berland, M. Yoon, S. Andersson, E. Schröder, P. Hyldgaard, and B. I. Lundqvist. Benchmarking van der waals density functionals with experimental data: potential-energy curves for h(2) molecules on cu(111), (100) and (110) surfaces. *Journal of physics. Condensed matter : an Institute of Physics journal*, 24(42):424213, Oct. 2012.
- [44] K. Lee, E. Murray, L. Kong, B. Lundqvist, and D. Langreth. Higher-accuracy van der waals density functional. *Physical Review B*, 82(8):3–6, Aug. 2010.
- [45] B. Li, X. Cao, H. G. Ong, J. W. Cheah, X. Zhou, Z. Yin, H. Li, J. Wang, F. Boey, W. Huang, and H. Zhang. All-carbon electronic devices fabricated by directly grown single-walled carbon nanotubes on reduced graphene oxide electrodes. *Advanced Materials*, 22(28):3058–3061, 2010.
- [46] G. Lü, R. Zhao, G. Qian, Y. Qi, X. Wang, and J. Suo. A highly efficient catalyst au/mcm-41 for selective oxidation cyclohexane using oxygen. *Catalysis Letters*, 97(3-4):115–118, 2004.
- [47] J. A. Mann and W. R. Dichtel. Noncovalent Functionalization of Graphene by Molecular and Polymeric Adsorbates. *The Journal of Physical Chemistry Letters*, 4(16):2649–2657, 2013.
- [48] H. Y. Mao, Y. H. Lu, J. D. Lin, S. Zhong, A. T. S. Wee, and W. Chen. Manipulating the electronic and chemical properties of graphene via molecular functionalization. *Progress in Surface Science*, 88(2):132–159, May 2013.
- [49] N. Marzari, D. Vanderbilt, A. De Vita, and M. C. Payne. Thermal contraction and disordering of the al(110) surface. *Phys. Rev. Lett.*, 82:3296–3299, Apr 1999.
- [50] H. J. Monkhorst and J. D. Pack. Special points for brillouin-zone integrations. *Phys. Rev. B*, 13:5188–5192, Jun 1976.
- [51] B. R. K. Nanda, M. Sherafati, Z. S. Popović, and S. Satpathy. Electronic structure of the substitutional vacancy in graphene: density-functional and green’s function studies. *New Journal of Physics*, 14(8):083004, 2012.

- [52] K. S. Novoselov, a. K. Geim, S. V. Morozov, D. Jiang, Y. Zhang, S. V. Dubonos, I. V. Grigorieva, and a. a. Firsov. Electric field effect in atomically thin carbon films. *Science (New York, N.Y.)*, 306(5696):666–9, Oct. 2004.
- [53] K. S. Novoselov, D. Jiang, F. Schedin, T. J. Booth, V. V. Khotkevich, S. V. Morozov, and a. K. Geim. Two-dimensional atomic crystals. *Proceedings of the National Academy of Sciences of the United States of America*, 102(30):10451–3, 2005.
- [54] W. S. Paz, W. L. Scopel, and J. C. Freitas. On the connection between structural distortion and magnetism in graphene with a single vacancy. *Solid State Communications*, (0):–, 2013.
- [55] J. Perdew, K. Burke, and M. Ernzerhof. Generalized gradient approximation made simple. *Physical review letters*, 77(18):3865–3868, Oct. 1996.
- [56] Z. Qian, J. Ma, X. Shan, L. Shao, J. Zhou, J. Chen, and H. Feng. Surface functionalization of graphene quantum dots with small organic molecules from photoluminescence modulation to bioimaging applications: an experimental and theoretical investigation. *RSC Advances*, 3(34):14571, 2013.
- [57] Y. Qiao, X.-S. Wu, C.-X. Ma, H. He, and C. M. Li. A hierarchical porous graphene/nickel anode that simultaneously boosts the bio- and electro-catalysis for high-performance microbial fuel cells. *RSC Advances*, 4(42):21788, 2014.
- [58] L. Qu, Y. Liu, J.-B. Baek, and L. Dai. Nitrogen-Doped Graphene as Efficient Metal-Free Electrocatalyst for Oxygen Reduction in Fuel Cells. *ACS Nano*, 4(3):1321–1326, 2010.
- [59] G. Román-Pérez and J. Soler. Efficient implementation of a van der waals density functional: Application to double-wall carbon nanotubes. *Physical Review Letters*, 103(9):1–4, Aug. 2009.
- [60] D. G. Saito R and D. M. S. Physical Properties of Carbon Nanotubes. *Imperial College Press*, 1998.
- [61] F. Schedin, a. K. Geim, S. V. Morozov, E. W. Hill, P. Blake, M. I. Katsnelson, and K. S. Novoselov. Detection of individual gas molecules adsorbed on graphene. *Nature materials*, 6(9):652–5, Sept. 2007.
- [62] F. Schwierz. Graphene transistors. *Nature nanotechnology*, 5(7):487–96, July 2010.
- [63] D. F. Shanno. Conditioning of Quasi-Newton Methods for Function Minimization. *Mathematics of Computation*, 24(111):647–656, July 1970.
- [64] Y. Shao, J. Wang, H. Wu, J. Liu, I. Aksay, and Y. Lin. Graphene Based Electrochemical Sensors and Biosensors: A Review. *Electroanalysis*, 22(10):1027–1036, May 2010.

- [65] A. Shytov, M. Rudner, N. Gu, M. Katsnelson, and L. Levitov. Atomic collapse, Lorentz boosts, Klein scattering, and other quantum-relativistic phenomena in graphene. *Solid State Communications*, 149(27-28):1087–1093, 2009.
- [66] J. Sławińska, P. Dabrowski, and I. Zasada. Doping of graphene by a Au(111) substrate: Calculation strategy within the local density approximation and a semiempirical van der Waals approach. *Physical Review B*, 83(24):1–8, June 2011.
- [67] S. J. Tans, A. R. M. Verschueren, and C. Dekker. Room-temperature transistor based on a single carbon nanotube. *672(1989):669–672*, 1998.
- [68] P. A. Thrower and R. M. Mayer. Point defects and self-diffusion in graphite. *physica status solidi (a)*, 47(1):11–37, 1978.
- [69] X. Tian, J. Xu, and X. Wang. Band gap opening of bilayer graphene by F4-TCNQ molecular doping and externally applied electric field. *The journal of physical chemistry. B*, 114(35):11377–81, 2010.
- [70] V. C. Tung, L.-M. Chen, M. J. Allen, J. K. Wassei, K. Nelson, R. B. Kaner, and Y. Yang. Low-temperature solution processing of graphene-carbon nanotube hybrid materials for high-performance transparent conductors. *Nano letters*, 9(5):1949–55, May 2009.
- [71] D. Vanderbilt. Soft self-consistent pseudopotentials in a generalized eigenvalue formalism. *Phys. Rev. B*, 41:7892–7895, Apr 1990.
- [72] M. Vanin, J. J. Mortensen, a. K. Kelkkanen, J. M. Garcia-Lastra, K. S. Thygesen, and K. W. Jacobsen. Graphene on metals: A van der Waals density functional study. *Physical Review B*, 81(8):1–4, Feb. 2010.
- [73] P. R. Wallace. The band theory of graphite. *Phys. Rev.*, 71:622–634, May 1947.
- [74] X. Wang, S. M. Tabakman, and H. Dai. Atomic layer deposition of metal oxides on pristine and functionalized graphene. *Journal of the American Chemical Society*, 130(26):8152–8153, 2008. PMID: 18529002.
- [75] X. Wang, L. Zhi, and K. Müllen. Transparent, conductive graphene electrodes for dye-sensitized solar cells. *Nano letters*, 8(1):323–7, Jan. 2008.
- [76] J. Winterlin and M.-L. Bocquet. Graphene on metal surfaces. *Surface Science*, 603(10-12):1841–1852, June 2009.
- [77] F. Xia, D. B. Farmer, Y.-M. Lin, and P. Avouris. Graphene field-effect transistors with high on/off current ratio and large transport band gap at room temperature. *Nano letters*, 10(2):715–8, 2010.

- [78] Z. Xu and M. J. Buehler. Interface structure and mechanics between graphene and metal substrates: a first-principles study. *Journal of physics. Condensed matter : an Institute of Physics journal*, 22(48):485301, Dec. 2010.
- [79] X. Yang, H. Wang, J. Li, W. Zheng, R. Xiang, Z. Tang, H. Yu, and F. Peng. Mechanistic insight into the catalytic oxidation of cyclohexane over carbon nanotubes: kinetic and in situ spectroscopic evidence. *Chemistry (Weinheim an der Bergstrasse, Germany)*, 19(30):9818–24, 2013.
- [80] D. Yu and L. Dai. Self-Assembled Graphene/Carbon Nanotube Hybrid Films for Supercapacitors. *The Journal of Physical Chemistry Letters*, 1(2):467–470, Jan. 2010.
- [81] W. J. Yu, S. Y. Lee, S. H. Chae, D. Perello, G. H. Han, M. Yun, and Y. H. Lee. Small hysteresis nanocarbon-based integrated circuits on flexible and transparent plastic substrate. *Nano letters*, 11(3):1344–50, Mar. 2011.
- [82] Y. Zhang and W. Y. Physical review letters 26 j anuary 1998 comment on “ generalized gradient approximation made simple ” in their recent letter , perdue , burke , and ernzerhof ( pbe ) [ 1 ] present a simplified version of the generalized-gradient approximation exchange-c. *Physical Review Letters*, 165(1993):9007, 1998.
- [83] Y.-H. Zhang, Y.-B. Chen, K.-G. Zhou, C.-H. Liu, J. Zeng, H.-L. Zhang, and Y. Peng. Improving gas sensing properties of graphene by introducing dopants and defects: a first-principles study. *Nanotechnology*, 20(18):185504, 2009.
- [84] J. Zhao, J. P. Lu, J. Han, C.-k. Yang, and J. Ping. Noncovalent functionalization of carbon nanotubes by aromatic organic molecules. *Appl Phys Lett*, 3746:30–33, 2003.
- [85] A. Zunger. Self-interaction correction to density-functional approximations for many-electron systems. 23(10), 1981.



# CURRICULUM VITAE

## PERSONAL INFORMATION

**Surname, Name:** Sayın, Ceren Sibel

**Nationality:** Turkish (TC)

**Date and Place of Birth:** 14.08.1984, Ankara

**Marital Status:** Single

**Phone:** 0 312 2107630

**Fax:** 0 312 2105099

## EDUCATION

<b>Degree</b>	<b>Institution</b>	<b>Year of Graduation</b>
M.S.	Middle East Technical University	2009
B.S.	Middle East Technical University	2007
High School	Tevfik Fikret Lisesi	2002

## PROFESSIONAL EXPERIENCE

<b>Year</b>	<b>Place</b>	<b>Enrollment</b>
2011-2014	Middle East Technical University	Research Assistant